J. Fluid Mech. (2005), *vol.* 538, *pp.* 153–187. © 2005 Cambridge University Press
doi:10.1017/S0022112005005276 Printed in the United Kingdom

The effect of bubbles on developed turbulence

By JUDITH RENSEN, STEFAN LUTHER AND DETLEF LOHSE

Department of Science and Technology and J. M. Burgers Center for Fluid Dynamics, University of Twente, PO Box 217, 7500 AE Enschede, The Netherlands

(Received 23 July 2003 and in revised form 13 March 2005)

Hot-film anemometry measurements are performed in a fully developed turbulent bubbly flow. For the bubble detection in the signal, both a threshold method and a new pattern recognition algorithm are employed. The measurements are carried out with gas fractions up to 3 % and a mean water velocity of $0.20\,\mathrm{m\,s^{-1}}$, corresponding to a Reynolds number of about 9×10^4. The typical bubble radius is 1–2 mm, corresponding to 10–20 Kolmogorov length scales. In this regime, a 'bubblance' parameter b which compares the kinetic energy originating from the rising bubbles with that of the turbulence fluctuations is smaller than 1. Probability distribution functions, structure functions (with and without the extended self-similarity (ESS) method), and spectra of the water velocity time series are calculated. Both our results for the turbulent energy spectra and the second-order structure functions show qualitative agreement with numerical results by Massitelli, Lohse & Toschi (Phys. Fluids, vol. 15 (2003), p. L5), i.e. a more pronounced energy enhancement on small scales than on large scales owing to the presence of bubbles, leading to a less steep slope in the spectrum as compared to the Kolmogorov $-5/3$ law. These results are robust, i.e. do not depend on details of the bubble detection scheme.

1. Introduction

1.1. *How do bubbles modify the turbulent energy spectrum?*

The statistics of velocity fluctuations in developed turbulence is well known from various experiments and numerical simulations. The probability distribution functions of velocity increments show an increasing flatness with decreasing length scale, reflecting the intermittent nature of the signal. Correspondingly, the scaling exponents of the velocity structure functions display (slight) intermittency corrections to the Kolmogorov results, and so does the scaling exponent $-5/3$ of the velocity power spectrum. For a summary of the present understanding, see Frisch (1995) and Pope (2000) or Sreenivasan & Antonia (1997).

This paper addresses the question how *bubbles* affect the velocity fluctuations in fully developed turbulent flow by performing hot-film anemometry in turbulent bubbly flow.

The reported results in the literature so far are inconclusive. The experiments of Lance & Bataille (1983, 1991), Wang *et al.* (1990) and Michiyoshi & Serizawa (1984) with relatively large bubbles of up to half a centimetre diameter show that, for an increasing gas fraction α, the Kolmogorov energy spectrum exponent $-5/3$ is progressively substituted by $-8/3$. It is argued that the steeper spectrum originates from immediate dissipation of the energy production within the bubble's wakes. In contrast, Mudde, Groen & van den Akker (1997), Mudde & Saito (2001) and Cui & Fan

(2004) found the classical $-5/3$ power law in a bubble column even for a gas volume fraction of 25 %. Mudde & Saito (2001) found this classical exponent $-5/3$ also for turbulent pipe flow. We have summarized a selection of previous results and our new experiments and numerical simulations in table 1. This table focuses on papers dealing with the spectral exponent; further numerical simulations on bubbly turbulence can be found in e.g. Climent & Magnaudet (1997, 99); Druzhinin & Elghobashi (1998); Murai & Matsumoto (2000); Druzhinin & Elghobashi (2001); Maxey, Chang & Wang (1994). For a summary of work up to 1995, we refer to Serizawa & Kataoka (1995).

1.2. *Results on the power spectrum*

Our main finding here will be a slightly less steep power spectrum as compared to the Kolmogorov $-5/3$ law. This result is in qualitative agreement to the numerical results by Mazzitelli, Lohse & Toschi (2003*a*, *b*) for microbubbles (diameter of several Kolmogorov scales η) in homogeneous nearly isotropic turbulence.

We realize that comparing the results of the numerical work with the current experiments poses several problems, owing to the different forcing conditions of the turbulence, to different degrees of turbulence and isotropy, and, in particular, to the larger bubble size in the experiments. However, in our experiments, the bubbles are still relatively small compared to inertial turbulent length scales, i.e. typically, about 10–20η for the bubble radius. Besides, we did not observe strong deformations of the bubbles. Therefore, we argue that the dominant effect of the bubbles is a rather localized forcing due to their buoyancy. Hence, comparing the current work with the numerical work of Mazzitelli *et al.* (2003*a*, *b*), which assumed a delta-type forcing due to the rising bubbles, is still useful.

There is, however, one qualitative difference between the presented experiments and the numerical simulations of Mazzitelli *et al.* (2003*a*, *b*): The simulations suggest that there is an energy input at small scales, but an energy *reduction* at large scales, which together lead to the less steep spectrum. The energy increase at the small scales is caused by the direct forcing through the bubbles, while the reduction of the energy at large scales is caused by a bubble accumulation at the downward flow side of the vortices, which is mainly a lift-force effect.

As stated already above, in the presented experiments we also find the less steep spectral slope, but it originates from a *strong* spectral enhancement at small scales and a *weaker* spectral enhancement at large scales. The reason for this difference is that in our presented experiments the massive injection of rising bubbles made it necessary to enhance the pump strength to guarantee a sufficiently large downflow velocity so that hot-film anemometry remains meaningful. The enhanced pump strength led to an energy enhancement on all scales. In contrast, in the numerical simulations the external large-scale forcing was kept fixed.

Van den Berg, Luther & Lohse (2005) have overcome this problem in a new series of experiments with the Twente water channel, where small concentrations of *microbubbles* (about 50 times smaller than the bubbles used here) were injected in the flow *upstream* and all other flow parameters were kept fixed. Indeed, then a *reduction* of the large-scale and an enhancement of the small-scale spectral power is found, just as in the numerical simulations by Mazzitelli *et al.* (2003*a*, *b*).

That the *overall* turbulence intensity can be reduced through the injection of bubbles has been known for a long time, see Serizawa, Tsuda & Michiyoshi (1975) and for a summary Serizawa & Kataoka (1995). The focus of this work is on the effect of the bubbles on the smaller scales and in particular on the spectrum.

Authors	Flow	Method	Re	Re_λ	R_b/m^m	Re_b	R_b/η	$\alpha(\%)$	b	Spectral exponent
Lance & Bataille (1983), Lance & Bataille (1991)	Grid generated turbulence, co-flow	Hot-film	1×10^4	35	3	700	6	0–3	0–15	$-5/3$ for small b, $-8/3$ for large b
Michiyoshi & Serizawa (1984)	Pipe flow	Hot-film						0–20		$\approx -8/3$
Wang *et al.* (1990)	Pipe flow	Hot-film	6×10^4					0–25		$\approx -8/3$
Mudde *et al.* (1997)	Bubble column	LDA	0	0	1.5	400	–	0–25	∞	$\approx -5/3$
Mudde & Saito (2001)	Pipe flow	Optical fibre	3×10^4		2	500		5.5	5	$\approx -5/3$
Mudde & Saito (2001)	Bubble column	Optical fibre	0	0	2	500	–	5.2	∞	$\approx -5/3$
Larue de Tournemine (2001)	Channel flow	Hot-film	7×10^4		1	250		0–8 %	0–15	$\approx -5/3$
Mazzitelli *et al.* (2003*a*, *b*)	Spectral Navier–Stokes code	Two-way coupling	–	60	0.1	1–6	1	0–1.6	0–0.02	Slightly less steep than $-5/3$
Mazzitelli & Lohse (2005)	Spectral Navier–Stokes code	Two-way coupling	0	0	0.1	2	–	0–3.2	∞	After transients $\approx -5/3$
Cui & Fan (2004)	Bubble column	LDA, PIV	0	0	3	700		0–20	∞	$\approx -5/3$
van den Berg *et al.* (2005)	Grid generated turbulence, co-flow	Hot-film	9×10^4	240	0.1	2	1	0–0.3	$0–2\times10^{-3}$	Slightly less steep than $-5/3$
Present work	Grid generated turbulence, counter-flow	Hot-film	9×10^4	240	1–2	250–500	10–20	0–3	0–1	Slightly less steep than $-5/3$

TABLE 1. Summary of experimental and numerical results on spectra in bubbly turbulence. Re is the flow Reynolds number without the bubbles, Re_λ the corresponding Taylor–Reynolds number, R_b is the bubble size, $Re_b = R_b U_R/\nu$ the bubble Reynolds number of a rising bubble in clean still water, η the Kolmogorov length scale, α the gas fraction, and b the bubblance parameter defined in (1.1). If data could not be extracted from the publication, we left the column blank. – The table does not aim at completeness.

1.3. *Bubblance parameter*

How do we explain that some measured spectra in bubbly turbulence such as those by Lance & Bataille (1991) show a steeper slope than $-5/3$, whereas others, including ours here, show a less steep slope? The differences in the various experiments and numerical simulations may be rationalized by differences in the employed bubble sizes and in the flow situations. In particular, it is important to compare the energy associated with the perturbations of the liquid through the bubbles with the typical turbulent kinetic energy in the absence of bubbles. The first energy is referred to as the pseudoturbulent contribution and is of the order of $\alpha C_A U_R^2$ (van Wijngaarden 1998), where $C_A = 1/2$ is the added mass coefficient and U_R is the rise velocity of bubbles in still water. The turbulent kinetic energy in the absence of bubbles is estimated by u'^2, where $u' = u'_z(\alpha = 0)$ is the typical vertical velocity fluctuation. We call the ratio of these kinetic energies 'bubblance' parameter b,

$$b = \frac{\frac{1}{2}\alpha U_R^2}{u_0'^2}. \tag{1.1}$$

For homogenous and (nearly) isotropic turbulence, the bubblance parameter b can be related to the often used parameter $\beta = u_0/U_R$, where u_0 is the large-scale r.m.s. velocity, namely $b \propto \alpha/\beta^2$. For $b < 1$, we are in the turbulence-dominated regime (with $b = 0$, no bubbles, in the limiting case), and for $b > 1$, we are in the pseudoturbulent regime where the flow is mainly driven by the rising bubbles (with $b = \infty$, bubbles in initially still water, as the other limiting case).

How are the values for the bubblance parameter b and the spectral slope correlated, if at all? In table 1, we have included our estimates for the bubblance parameter b for the various experiments and numerical simulations. For $b < 1$, Lance & Bataille (1991) found a power law exponent of $-5/3$. This power law exponent is progressively substituted by $-8/3$ when the pseudoturbulent contribution becomes dominant, $b > 1$. The measurements of Mudde *et al.* (1997) are restricted to the wall region, where turbulence production is strong, presumably leading to a turbulence dominated regime. Also in the case of Mazzitelli *et al.* (2003*a*, *b*) we have $b < 1$, as the turbulence is relatively strong and only microbubbles with a slow rise velocity are injected. The experiments presented in this paper will also turn out to have a bubblance parameter $b < 1$, i.e. we are in the turbulent-dominated regime and we expect that the bubbles modify only the spectra and structure functions.

So, can the regime $b < 1$ be associated with a spectral slope (close to) $-5/3$ and the regime $b > 1$ with a spectral slope (close to) $-8/3$? From table 1, we clearly have to conclude that this is not the case. The bubble column experiments in table 1 all start with the fluid at rest; the flow is excited exclusively by the rising bubbles, i.e. $b = \infty$. Nonetheless, the spectral slope is close to $-5/3$. The same holds for the pseudoturbulence simulation of Mazzitelli & Lohse (2005). So there must be further yet unknown conditions for the $-8/3$ regime to occur. We will come back to this in the conclusions.

1.4. *Results on probability density functions (PDFs) and on velocity structure functions*

Apart from in the spectrum, the modifications of the velocity fluctuations by the bubbles will also reflect in further statistical observables.

(i) The velocity structure functions of second order are basically the Fourier transformation of the power spectrum (Pope 2000). We therefore also find a decreased

slope as compared to the Kolmogorov value 2/3. Note that in practice, the Fourier-transformation from the spectrum to the second-order structure function is difficult because of finite size effects (Lohse & Müller-Groeling 1995, 1996).

(ii) Higher-order velocity structure functions show slightly enhanced intermittency in bubbly flow as compared to single-phase flow. Since the structure functions as a function of the length scale r show only poor scaling properties for the low Reynolds numbers of most experiments, including ours here, we have to analyse the so-called extended self-similarity (ESS) plots, where one structure function is plotted versus another one (Benzi *et al.* 1993; Briscolini *et al.* 1994). For visualization of different intermittency, *compensated* extended self-similarity plots have turned out to be useful (Grossmann, Lohse & Reeh 1997*b*, *a*).

(iii) Another important finding is that the extended self-similarity property vanishes in two-phase flow, owing to the small-scale energy input by the bubbles.

(iv) The most direct way to access intermittency is to measure the probability density functions (PDF) of the velocity increments. The intermittency shows up in increasing tails of the PDF with decreasing length scale, see e.g. Belin, Tabeling & Willaime (1996). Here the enhanced intermittency of bubbly flow as compared to single-phase flow reflects in more pronounced wings of the PDFs of the small-scale velocity increments. Note that the tails of the PDFs are probed by high-order velocity structure functions and the peak is probed by low-order velocity structure functions.

1.5. *Signal processing*

The main problem in turbulence bubbly flow is the velocity data acquisition. We chose hot-film anemometry as it can be applied even if the gas-fraction is of the order of a few per cent. In contrast to laser-Doppler anemometry (LDA) and particle image velocimetry (PIV), the data rate that can be obtained in the bulk of bubbly flow is still sufficient to estimate energy spectra. (Note, however, that very close to the boundaries of bubbly flow, LDA has successfully been used (Mudde *et al.* 1997).)

However, hot-film anemometry also has various problems in turbulent bubbly flow. The most serious problem is the appearance of disturbances in the hot-film signal owing to bubble–probe interactions. These spiky structures in the hot-film signal are caused by the interaction between the hot-film probe and the bubbles and do not contain information on the water velocity. They simply reflect that the heat conductivity of the bubbles touching the probe is less than that of the water. We test two methods of bubble spike detection: a common threshold method and a new pattern-recognition method by Luther & Rensen (2004) and Luther *et al.* (2005). None of these methods is perfect; however, the results we obtain are robust.

We may hope that applying the ESS method to probe signals with some remaining bubble signatures may help, as the effect of bubbles in velocity structure functions of different order may cancel out. However, we will show that the bubble signatures in the signal affect different velocity structure functions in different ways, so that this method cannot be used here.

A second less serious problem of hot-film anemometry in bubbly flow is the need for signal-processing algorithms that are able to estimate structure functions, PDFs and spectra while some data points of the time series are missing, namely those periods when a bubble had touched the probe, thus corrupting the signal. We will offer solutions to this problem in this paper.

Finally, the calibration of the hot-film anemometer is changing on a time scale of minutes because of pollution of the sensing element. We overcome this problem by a continuous calibration of the hot-film anemometer.

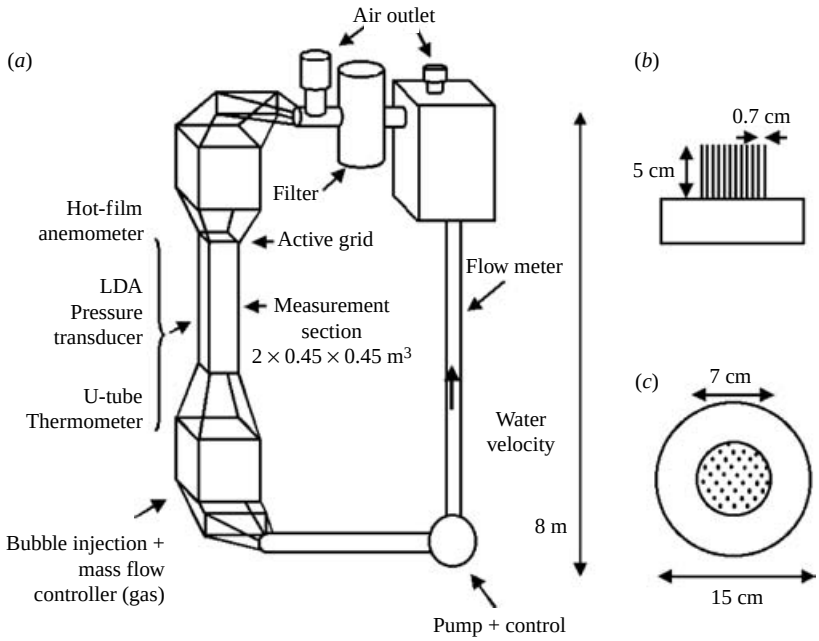

FIGURE 1. (*a*) Schematic picture of the Twente water tunnel. (*b*, *c*) Side and top view of a bubble injection island. Nine of these islands are installed at the bottom of the channel.

1.6. *Organization of the paper*

The structure of this paper is as follows. In § 2, the experimental set-up and the instrumentation are described. In § 3, we introduce the signal-processing algorithms and discuss their robustness and accuracy. The main findings and results on PDFs, structure functions and spectra are presented in § 4. An extended summary, conclusions and an outlook are given in § 5.

2. Experimental set-up and measurement techniques

2.1. *Water tunnel*

The water tunnel is depicted in figure 1. The tunnel has a measurement section with a cross-section of $L \times L = 0.45 \times 0.45\,\mathrm{m}^2$ and a height of 2 m. Deionized water is pumped vertically downwards through the measurement section by a 17.6 kW elbow pump (Egger RPP 300). The angular speed of the pump propeller is controlled by a frequency converter (Danfoss VLT 175 H 1238ST). The mean water velocity is measured by an electromagnetic flow meter (Danfoss Magflo Mag3100). A filter (Spirotech Spirovent) has been installed to diminish pollution of the water. Volume flow rates up to $0.1\,\mathrm{m}^3\,\mathrm{s}^{-1}$ can be achieved. The water tunnel is supplied with an active computer-controlled grid that enhances the turbulent intensity. Owing to the active grid, large Taylor–Reynolds numbers up to $Re_\lambda = 200$ can be achieved while the transverse homogeneity of the flow remains satisfactory. In figure 2, we can see the power spectral density of the vertical velocity of a single-phase flow in the tunnel measured by hot-film anemometry. The figure shows a nearly constant scaling exponent of about $-5/3$ over almost two decades. For more details on the tunnel and the active grid, we refer to the work of Poorte (1998) and Poorte & Biesheuvel (2002).

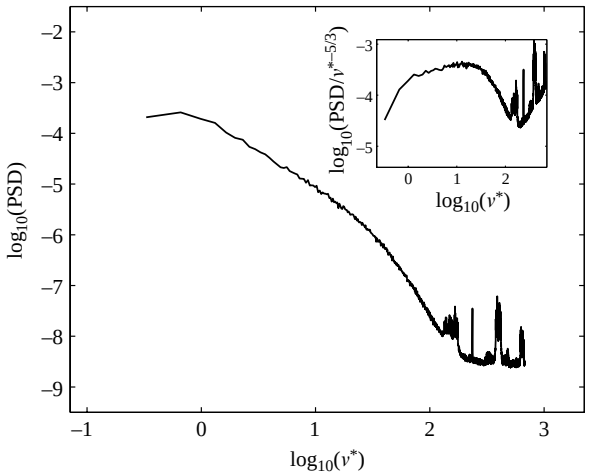

FIGURE 2. Power spectral density plot and compensated power spectral density plot (inset) *vs.* the dimensionless frequency $\nu^* = \nu U_z/L$ for a single-phase flow with $Re \approx 9 \times 10^4$. ν is the frequency, L the width of the tunnel and U_z the average water velocity.

Below the measurement section, air bubbles are injected by orifices. The size of the bubbles is controlled by mass-flow controllers (MKS 1559A) with ranges from 1 up to 100 slm (standard litre per minute) and by the sizes of the orifices (Oguz & Prosperetti 1993). The orifices have lengths of 5 cm and inner diameters of 0.5 mm. In total, 621 orifices are distributed over 9 islands, see figure 1. The air supply to every island can be switched on or off separately. The islands are installed in a 3×3 matrix below the contraction under the measurement section. The bubble size and the flow velocity are chosen such that most of the bubbles rise upwards. Gas fractions up to 10 % can be achieved. Measurements with a four-point optical probe showed that the diameters of the bubbles $D_b = 2R_b$ are in the range of 2 to 5 mm. The relative rise velocity U_R of the bubbles is assumed to be about $0.23\,\mathrm{m\,s^{-1}}$ (Clift, Grace & Weber 1978). Validation of the homogeneity of the mean flow velocity after the installation of the islands has been successfully performed using LDA.

2.2. *Measurement techniques*

We used a Dantec constant-temperature hot-wire anemometer system (90N10 frame and 90C10 module) and the Dantec streamware software (V2.05) to measure the local vertical water velocity in the measurement section. We used a Dantec 55R11 hot-film probe, which has a cylindrical quartz rod with a diameter of 70 μm diameter, a total length of 3 mm, and a sensitive length of 1.3 mm. Owing to the boundary layer and the protective quartz coating, the frequency bandwidth is limited to about 1 kHz. The hot-film probe was mounted in the centre of the measurement section of the tunnel 50 cm below the active grid. The signal of the hot-film probe was sampled with 6 kHz at a resolution of 12 bits by an AD-card (National Instruments BNC-2090 and PCI-E6023). This relatively high sampling rate was chosen because we had initially hoped to be able to measure relatively high frequencies in the signal. The hot-film anemometer was calibrated with a Dantec backscatter LDA system. We used a 4 W Argon ion laser (Spectra Physics Stabilite 2017). The bursts were analysed using Dantec software (BSA flow V1.4).

The temperature of the water was monitored by the temperature probe of the stream-ware system and by a Silicon PTC temperature sensor. To determine the

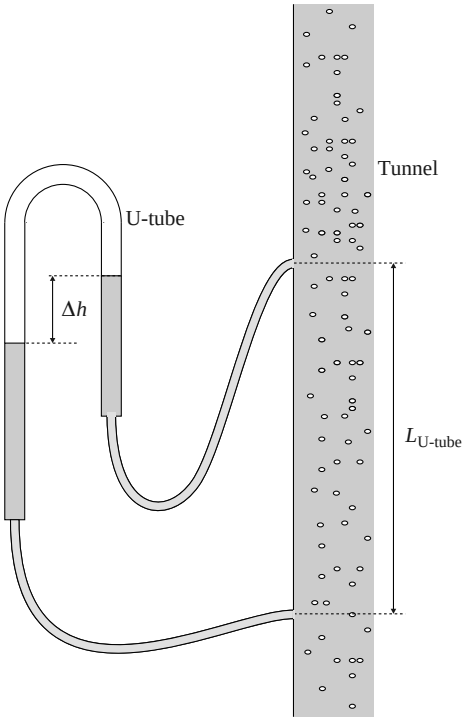

FIGURE 3. U-tube set-up to measure the gas fraction α. The distance between the two connection points between the U-tube and the channel is $L_{U\text{-}tube}$, and the difference in the water column height in the U-tube is Δh.

gas fraction, the pressure difference between two points at different heights in the measurement section was measured. A U-tube was used for this purpose (figure 3). As the flow is homogeneous and the velocity along the channel is constant, the gas fraction can be obtained as

$$\alpha_{U\text{-}tube} = \Delta h / L_{U\text{-}tube},$$

where Δh and $L_{U\text{-}tube}$ are defined in figure 3.

To measure the typical size distribution of the bubbles produced by the islands, a four-point optical-probe (Mudde & Saito 2001) was used. As the probe was at our disposal for only a short period of time, it was not used during the final experiments which produced those velocity time series on which the data in this paper are based.

Despite several measures to prevent electrical noise, some noise was still present in the hot-film signals. Most of the energy content of the remaining noise was in frequencies higher than those we were interested in, and therefore the remaining noise did not have a significant effect on the spectra and PDFs. In order to obtain well-behaved structure functions in the small-scale regime, we filtered out the remaining noise by a 10th-order Butterworth low-pass filter. The cutoff frequency of the filter was set at 300 Hz.

2.3. *Measurement conditions*

2.3.1. *Flow parameters*

The parameters of our various experiments with different volume fraction of bubbles are summarized in table 2. We used a volume flow rate of $4 \times 10^1\,\mathrm{l\,s^{-1}}$,

U_z (m s^{-1})	Re	α (%)	u'_z (m s^{-1})	$\frac{u'_z}{U_z}$	L_{11} (m)	λ_f (m)	η (m)	ϵ (m^2 s^{-3})	b
0.20	8.9×10^4	0	0.026	0.13	0.076	0.0092	1.5×10^{-4}	0.0020	0
0.20	9.0×10^4	0.5	0.033	0.17	0.018	0.0041	1.2×10^{-4}	0.0052	0.2
0.20	9.1×10^4	0.7	0.035	0.17	0.029	0.0039	1.1×10^{-4}	0.0060	0.3
0.21	9.6×10^4	1.0	0.039	0.18	0.049	0.0038	1.1×10^{-4}	0.0081	0.4
0.21	9.5×10^4	1.5	0.047	0.22	0.067	0.0038	9.4×10^{-5}	0.013	0.6
0.20	8.8×10^4	2.0	0.052	0.27	0.068	0.0035	9.0×10^{-5}	0.015	0.8
0.20	8.8×10^4	2.9	0.079	0.40	0.084	0.0036	7.3×10^{-5}	0.036	1.1

TABLE 2. Flow parameters: U_z is the mean vertical downward water velocity, α the gas fraction, u'_z is the standard deviation of the vertical water velocity, L_{11} is the longitudinal integral length scale, λ_f is the Taylor microscale, η is the Kolmogorov length scale, ϵ is the dissipation rate, and b is the bubblance parameter defined in (1.1). The typical bubble radius is always $R_b = 1 - 2$ mm, i.e. typically, 10–20η.

which corresponds to a mean downward vertical velocity in the measurement section of 0.2 m s^{-1}. The Reynolds number Re of this flow was of the order of 9×10^4. The bubble Weber number was about 2 and the bubble Reynolds number is about 5×10^2. The Kolmogorov length η was of the order of 10^{-4} m. By the choice of the mean vertical velocity, we considered the following. The mean vertical velocity, should not be higher than the bubble slip velocity, as we wanted the bubbles to rise upwards. Besides, we had to take into account the fact that a hot-film anemometer only measures absolute velocities. This means that any upward velocity of the water in the tunnel should be avoided. Therefore, the condition $u'_z/U_z \ll 1$ must be fulfilled, where U_z and u'_z are, respectively, the mean and the standard deviation of the vertical water velocity. Furthermore, we wanted to apply Taylor's hypothesis, see also § 3.4, which can also only be used under the condition that $u'_z/U_z \ll 1$. On the other hand, the mean vertical water velocity U_z had to be much larger than the mean horizontal velocities U_x and U_y, as otherwise the velocity measured by the hot-film anemometer will be biased. In addition, high Reynolds numbers and thus high values of U_z, are desired to be able to measure turbulent properties such as, for example, scaling exponents. The velocity chosen is a compromise of the preceding requirements, which are partly contrary to each other. For the experiments described in this paper, gas fractions up to 2.9 % were used. Higher gas fractions were avoided as these would have caused $u'_z/U_z \approx 1$, which can be seen in figure 4. Besides, the data rate of the LDA would have become too low to obtain a well-converged PDF of the water velocity as measured by the LDA.

The bubblance parameter b given in table 2 is always smaller than one, signalling that the turbulence is only modified by the bubbles, but not dominated by the kinetic input due to the rising bubbles, as would be the case in pseudoturbulence. The table also shows that the bubbles have a radius of about 10–20η. The size of the bubbles is thus not too far from the viscous subrange.

2.3.2. *Measurement time and convergence*

How long must we measure to obtain well-converged velocity structure functions of order p in turbulent bubbly flow? Whenever a bubble is passing in the neighbourhood of the hot-film probe, a violent change in the hot-film signal is observed, either because of the change in the heat-transfer when a bubble touches the probe, or owing to the local velocity field around a bubble. As we used gas fractions of the order of a few

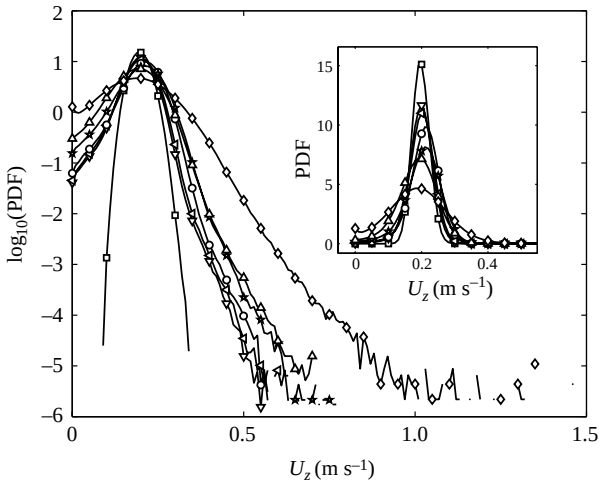

FIGURE 4. PDF of U_z for a flow with $Re \approx 9 \times 10^4$ and gas fractions of $\alpha = 0\,\%$ (squares), $\alpha = 0.5\,\%$ (triangles down), $\alpha = 0.7\,\%$ (triangles left), $\alpha = 1.0\,\%$ (circles), $\alpha = 1.5\,\%$ (pentagrams), $\alpha = 2.0\,\%$ (triangles up), and $\alpha = 2.9\,\%$ (diamonds). The data have been obtained by hot-film anemometry.

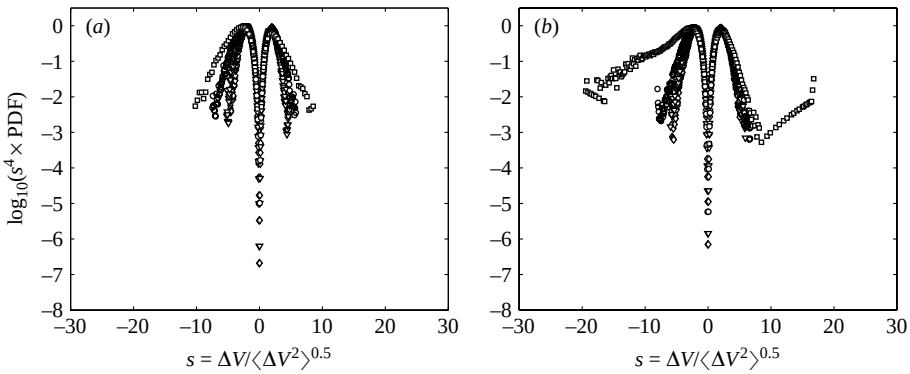

FIGURE 5. PDFs of the velocity increments $s = \Delta U_z(r_z)/\langle(\Delta U_z(r_z))^2\rangle$, multiplied by s^4, for (*a*) single-phase flow with $Re \approx 9 \times 10^4$ and (*b*) bubbly flow with $Re \approx 9 \times 10^4$ and $\alpha = 2.9\,\%$ on the scales $r_z \approx 8\eta$ (squares), $r_z \approx 64\eta$ (circles), $r_z \approx 512\eta$ (triangles) and $r_z = L = 4500\eta$ (diamonds). To detect the bubbly spikes in the signal, the threshold method was applied (see § 3.3.1). For both cases, the statistics is sufficient to obtain convergence of fourth-order moments $\propto \int s^4\, PDF(s)\, \mathrm{d}s$.

per cent, the changes in the signal only occur during a small fraction of the total measurement time, i.e. these are rare events. Consequently, in order to obtain well-converged moments, much longer time series are required in bubbly flow as compared to single-phase flow. We performed measurements of 100 min for the single-phase-flow situation and measurements of 150 to 250 min for the two-phase-flow situation. Inspection of the PDFs of the higher moments of the velocity increments showed that, for single-phase flow, this is absolutely sufficient to have well-converged sixth-order moments, but for bubbly flow, we are only able to obtain well-converged fourth-order velocity structure functions. In figure 5(*a*), the PDFs, weighted by the velocity increments to the fourth power, are shown as a function of the increment for a single-phase

flow and in figure 5(*b*) for a bubbly flow with $\alpha = 2.9\,\%$. The bubbly spikes in the signals were removed before calculating the PDFs. Even on the smallest scales, that plot displays clear maxima, and thus fourth-order moments can be calculated.

3. Signal processing

The classical method for detecting bubbles in a hot-probe signal is a threshold method (Bruun 1995), in which all spikes in the derivative of the signal which are larger than a threshold are defined as 'bubbly spikes'. As pointed out by Luther & Rensen (2004), threshold methods on the derivative cannot detect all bubbles in the hot-film signal for our type of measurements because of the overlap in the PDF of the derivatives of the hot-film signal of bubbly spikes and of the fluid signal itself. This will be further discussed in § 3.3.3. Nevertheless, we decided to apply this method so that we could make a comparison with previous work, in which threshold-based methods have been used extensively. The alternative method which we will employ is the pattern-recognition scheme developed in Luther & Rensen (2004). We will show here that both methods essentially lead to the same physical conclusions, though the detailed numbers will differ slightly. Before we elaborate on the bubble-detection schemes, in the next subsection we report on the probe calibration.

3.1. *Calibration*

Hot-film anemometry is based on the relation between the heat convection from an electrically heated sensing element to a surrounding flow and the velocity of this flow (Bruun 1995). The heat flux from the sensing element is described by King's law

$$E_{HF}^2 = A + Bu_z^n, \tag{3.1}$$

where E_{HF} is the voltage over the sensing element of the probe, u_z is the local vertical flow velocity, and A, B and n are constants that must be obtained by calibration. A problem with the calibration of hot-film probes is that the heat flux from the measuring part to the surroundings is very sensitive to temperature changes of the flow and to contamination of the sensing element. This means that the calibration of our hot-film probe was changing on a time scale of minutes. These changes were caused mainly by pollution of the sensing element as the water temperature was changing very slowly, because of the large heat capacity of the water and the moderate changes in ambient temperature. Furthermore, sometimes a jump in the hot-film signal occurred. These jumps were caused by cleaning of the sensing element by bubble–probe interactions. These changes in the calibration had to be taken into account, since we had to carry out long measurements to obtain statistically well-converged results. For this purpose, we carried out LDA and hot-film measurements simultaneously. The data rate of the LDA system was rather low, because of the presence of bubbles in the optical path. However, thanks to the long duration of the measurements, at least 400 samples for each data set could be collected. We used the PDF obtained by fitting a Gaussian probability function to the normalized histogram of the LDA velocity data, to calibrate the hot-film anemometer. The hot-film signal was divided into parts with a duration of 2 min. For every time interval, a separate calibration curve was obtained by minimizing the difference between the PDF of the water velocity as obtained by the LDA measurement and the PDF of the water velocity as obtained by the hot-film measurement. Equation (3.1) was used as a calibration function. The variables A, B and n were used as the fitting parameters for the minimization algorithm. Whenever sudden changes in the mean hot-film

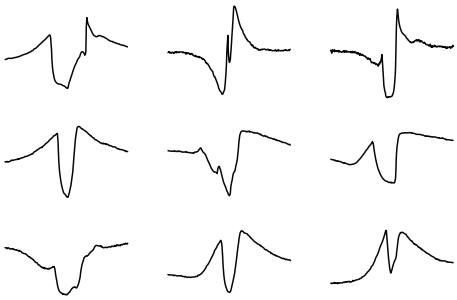

FIGURE 6. Typical examples of hot-film signals during bubble–probe interaction. In the figures, time is plotted on the horizontal axis and the voltage on the vertical axis. The duration of the shown signals is about 0.05 s.

signal were observed, the corresponding two minute time intervals were excluded from further signal processing. The sudden changes were detected by inspection of a running average of the hot-film signal. Also the bubbly spikes in the signal, as detected by the methods to be described in § 3.3, were excluded from the calibration procedure.

3.2. *Bubble–probe interaction*

The interaction between a hot-film probe and bubbles had already been investigated by several workers (Delhaye 1969; Bremhorst & Gilmore 1976; Serizawa, Tsuda & Michiyoshi 1983; Farrar & Bruun 1989; Bruun 1995). However, the case in which bubbles rise upstream has, to our knowledge, not yet been considered. Hence, we decided to study the bubble–probe interactions with the help of stereoscopic high-speed imaging, simultaneously measuring the probe response. In this way, we obtained a series of examples of the hot-film signal during bubble–probe interaction. In figure 6, some of these examples can be seen. We may hope that specific features of these signals are correlated with the dynamical interaction process between bubble and probe, namely, to deduce from the hot-probe signal whether the bubble is penetrating the probe, bouncing from it, or being split; however, we failed to find such correlation (Rensen *et al.* 2004). The examples shown in figure 6 could, in principle, be used to 'train' the neural-network-type pattern-recognition scheme. We indeed tried to do so, but as the flow in Rensen *et al.* (2004) is laminar and not turbulent as the flow we want to analyse here, we eventually decided to create the training set in a different way, see below.

The second result we obtained from the measurement in Rensen *et al.* (2004) is that the determination of the gas-fraction as described in Bruun (1995) is not applicable in our flow situation. For details on those experiments and the results of the stereoscopic imaging, we refer to Rensen *et al.* (2004).

The third result of the stereoscopic imaging of rising bubbles interacting with hot-film probes has already been published (de Vries *et al.* 2002*b*). In that paper we had focused on the bubble-shape oscillations induced by the interaction with the probe, which resulted in oscillations in the bubble rise velocity, and in velocity fluctuations of the water around the bubble.

3.3. *Bubble detection*

To allocate the spikes caused by the bubble–probe interactions, two different methods were used. The first was a threshold method and the second a pattern-recognition algorithm. Results of both bubbly-spike detection methods are shown in figure 7.

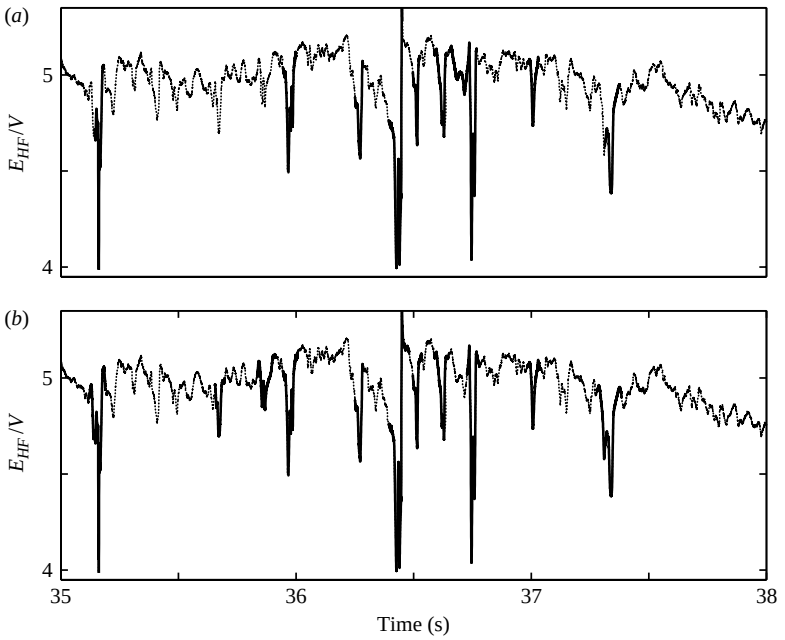

FIGURE 7. Detected bubbly spikes (solid lines) in a hot-film signal (dotted line) of a bubbly flow with $Re = 9 \times 10^4$ and a gas fraction of 1.0 %. (*a*) Results for the case where pattern recognition was applied to detect the bubbly spikes. (*b*) Results for the case where the threshold method was applied.

Though most of the detected events are found with both methods, there are some events – be they caused by bubble–probe interactions or be they intermittent bursts – that are only found by one of the methods. We will now introduce the two employed methods and explore whether the different features in the bubble-recognition methods are relevant from a statistical point of view.

3.3.1. *Threshold method*

The threshold method detects the bubbly spikes in the signal by a threshold on the derivative of the signal. A typical hot-film signal of a passing bubble contains a sudden decrease of the voltage if a bubble arrives at the probe and a sudden increase of the voltage as it leaves the probe (see figure 6). The threshold method assumes that a bubble is present at the hot-film probe if the derivative of the signal is below a certain negative value. Comparable methods sometimes combined with a threshold on the amplitude were used by Marié, Moursali & Tran-Cong (1997), Lance & Bataille (1991), Panidis & Papailiou (2000) and Wang & Ching (2001).

The key quantity for the threshold method is obviously the value of the chosen threshold, aiming at a satisfactory detection performance. We tried various values for the threshold. The influence of the exact threshold value on the structure functions, the ESS plots, and the power spectral density (PSD) is depicted in figures 8 and 9. The figures show that the influence of the value of the threshold on the second-order structure functions and the PSD is limited. In contrast, the influence of the value of the threshold on the ESS plots and the fourth-order structure functions is more pronounced.

Eventually, we took $26.4\,\mathrm{Vs}^{-1}$ as threshold value for the derivative. This value is based on the following consideration. In figure 10, the PDFs of the minima of the

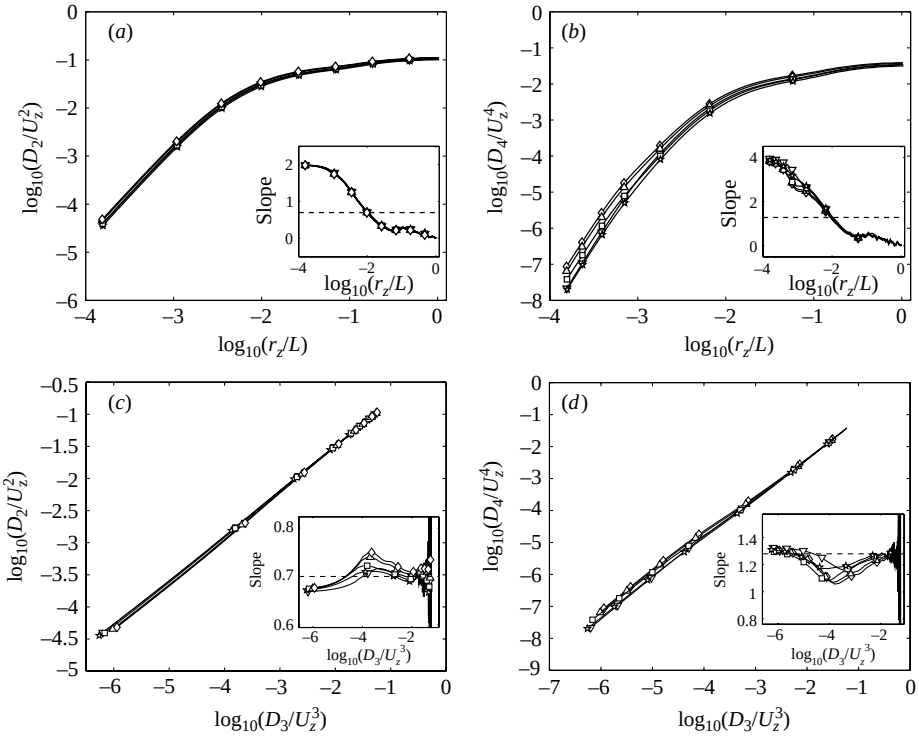

FIGURE 8. Results for a flow with $\alpha = 1.5\,\%$ and $Re \approx 9 \times 10^4$ in the case where the used threshold to find the bubbly spikes was $-21.6\,\mathrm{Vs}^{-1}$ (pentagram), $-24.0\,\mathrm{Vs}^{-1}$ (squares), $-26.4\,\mathrm{V/s}$ (triangles down), $-28.8\,\mathrm{V/s}$ (triangles up), $-31.2\,\mathrm{V/s}$ (diamonds). (*a*) Plot of D_2/U_z^2 *vs.* r_z/L and its local slope (inset). The dashed line corresponds to a slope of 0.7, which is the typical value given for the (intermittent) scaling of the second-order structure function. (*b*) Plot of D_4/U_z^4 *vs.* r_z/L and its local slope (inset). The dashed line corresponds to a slope of 1.28, again the typical (intermittent) scaling exponent for fourth-order structure functions. (*c*) Extended self-similarity (ESS) plot of D_2/U_z^2 *vs.* D_3/U_z^3 and its local slope (inset). The dashed line corresponds to a slope of 0.7. (*d*) ESS plot of D_4/U_z^4 *vs.* D_3/U_z^3 and its local slope (inset). The dashed line corresponds to a slope of 1.28.

derivatives of the bubbly-spike training data (to be defined below) and the minima of the derivatives of the water training data are shown. As the PDFs show some overlap, it is not possible to choose a value for the threshold that gives an entirely correct recognition. However, by decreasing the value of the threshold, more water and fewer bubbles would be recognized correctly. As later it is shown that non-detected bubbly spikes do have a large influence on the ESS plots and the spectra, we prefer to select a threshold that recognizes the bubbly spikes correctly rather than the water parts of the signal. With the threshold value $26.4\,\mathrm{Vs}^{-1}$ (dashed line), this property is achieved.

3.3.2. *Pattern recognition*

The pattern-recognition algorithm is based on the observation that bubble–probe interactions result in a typical pattern or shape of the hot-film signal (Luther & Rensen 2004). The algorithm consists of an optimal signal decomposition using adaptive wavelet transform (Saito & Coifman 1994) and a classification of the decomposed data by a neural-network-based trained classifier (Kohonen 1995). The algorithm requires training data, i.e. data sequences from which it is known that they belong

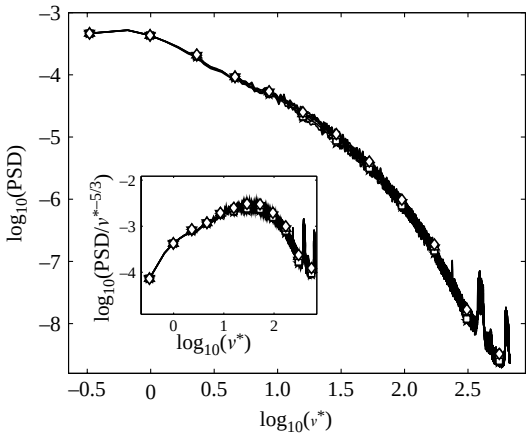

FIGURE 9. Power spectral density (PSD) and compensated PSD (inset) vs. the dimensionless frequency $\nu^* = \nu U_z/L$ of a flow with $\alpha = 1.5\,\%$ and $Re \approx 9 \cdot 10^4$ in case that the used threshold to find the bubbly spikes was −21.6 V/s (pentagram), −24.0 V/s (squares), −26.4 V/s (triangles down), −28.8 V/s (triangles up), −31.2 V/s (diamonds). Hardly any difference between the curves is seen.

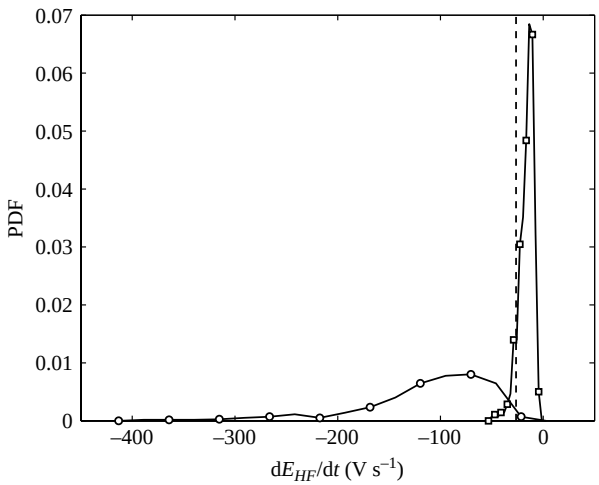

FIGURE 10. The PDF of the minimum of the derivative of manually selected hot-film signal parts of bubble-probe interactions (circles) and the PDF of the minimum of the derivative of manually selected hot-film signal parts that belong to the water phase (squares) of a flow with $\alpha = 2.9\,\%$ and $Re \approx 9 \times 10^4$. The dashed line corresponds to the threshold value of $26.4\,\mathrm{Vs}^{-1}$ that is used in the threshold method for bubble detection.

either to bubbly spikes or to water velocity signal parts. We obtained the training data by selecting by eye – based on our experience with simultaneous stereoscopic imaging and probe-signal detection reported in § 3.2 – at least 400 data signal parts belonging to bubble–probe interactions and 400 data signal parts belonging to the water phase for each measurement series. The algorithm was trained for each measurement series separately using the corresponding training data set. The trained algorithm is finally used to detect bubble spikes in hours of probe data series.

Obviously, the selection of training data by eye may give erroneous sets of training data, in particular, as our experience is built on simultaneous stereoscopic imaging

	Threshold method		Pattern recognition	
Gas fraction	Bubbles	Water	Bubbles	Water
0.5	98.1	98.6	99.2	90.5
0.7	97.1	99.6	100	85.9
1.0	99.0	97.9	99.0	74.5
1.5	98.9	92.4	99.1	83.3
2.0	99.3	92.2	98.9	81.3
2.9	99.6	90.9	99.6	82.9

TABLE 3. The percentages of correctly recognized signal parts for flows with different gas fractions.

and probe-signal detection in a flow with much smaller Reynolds number (Rensen *et al.* 2004). A better way would be to perform simultaneous hot-probe and optical fibre measurements *at the same position* so that we know for sure whether a bubble had been around or not. We are working on such a set-up, but as we will show in the following, the present results are already robust and reliable.

3.3.3. *Validation*

To validate both bubble-detection algorithms, we used the training data of the pattern-recognition algorithm. The training data of both the bubbly parts and the water parts of the signal were separately fed into both algorithms. For each class, the percentage of correctly recognized bubbles was determined. The results are summarized in table 3.

The percentages of 98 % to 99 % bubbly-spike detection for both methods appear to be very promising. However, the recognition of the water parts by the pattern recognition method is less accurate than by the threshold method. This is probably because the pattern recognition assumes that the water velocity can be represented by a typical pattern, which may be a misconception. For the same reason, probably fewer water parts are recognized correctly by the pattern-recognition method than bubbly spikes. The table shows that the water detection by the threshold method is also less accurate than the bubbly-spike detection by this method.We stress again that our focus must be on correct bubble detection, as non-detected bubble spikes have a larger impact on PDFs and structure functions than water parts taken out of the signal erroneously.

At the moment, it is not possible to give a more accurate estimate of the accuracy of both bubbly-spike-detection algorithms for the turbulent two-phase-flow measurements in the tunnel. Validation of the presence of a bubble on the probe by optical inspection from outside the tunnel is not possible, because the bubbles block the optical path. Also, using the gas fraction estimate from the hot-film data, like Lance & Bataille (1991) did, is not reliable in our case, as we (Rensen *et al.* 2004) showed that the hot-film does not give the correct gas fraction in our application.

What are the long-term prospects of the two methods employed? The threshold method cannot be improved as figure 10 shows overlap between the two distributions. In contrast, from our point of view, the pattern-recognition method has more potential as it can be further improved, e.g. by using other training data, or by adapting it in such a way that it does not assume that the water parts of the signal can be represented by a typical pattern. As stated above, the only way to obtain suitable training data is to supply the hot-film probe with a second measurement device that is

capable of distinguishing bubbles from water, such as an optical fibre, and to obtain training data in that way. (Of course, if such a combined device can be realized and used during the whole measurement, a bubbly-spike-detection algorithm will no longer be required.)

3.3.4. *Gas fraction and dead-time fraction estimate*

Both the threshold method and the pattern-recognition method give only the data point in the signal around which a bubbly spike is located. Once these positions are detected, the beginning and the end of the distortion must still be determined. The beginning of a distortion was set at 8 ms before the beginning of the falling flank in the neighbourhood of the found bubbly-spike location that showed the largest decrease of the hot-film signal. The end point was set at 8 ms after the end of the rising flank that followed the beginning of the spike and that showed the largest increase of the hot-film signal. The buffers of 8 ms were used to correct for small misdetections in the determination of the beginning and the end of a bubbly spike. Assuming that the bubble rise velocity relative to the water was of the order of $25\,\mathrm{cm\,s^{-1}}$ (Clift *et al.* 1978) and that the downward water velocity was $20\,\mathrm{cm\,s^{-1}}$ relative to the probe, a bubble only travelled a distance of the order of 0.4 mm with respect to the probe in this period. This is about a factor of 10 smaller than the bubble size. Therefore, we do not expect to lose substantial parts of the water velocity data of the bubbles' wakes owing to the use of the buffer. The influence of the length of the buffer can be seen in figure 11. The figure shows that the results converge for buffer times longer than 4.2 ms.

The dead-time of a bubble–probe interaction signal is defined as the time between the beginning and the end of the distortion. The residence time of a single bubble is the time between the beginning of the falling flank and the beginning of the rising flank that were used in the determination of the dead-time of the signal. The dead-time fraction and the gas fraction can be derived by summing all dead-times and residence times and dividing them by the total measurement time (Bruun 1995). In figure 12, the gas fraction and the dead-time fraction of the signal obtained from the hot-film signals by the threshold method and the pattern recognition are shown as function of the gas fraction measured by the U-tube. For both methods, there is a roughly linear relation between both the gas fraction and the dead-time fraction and the gas fraction measured by the U-tube. However, the gas fraction obtained from the hot-film signal is a factor of about 4 higher than the gas fraction measured by the U-tube.

What is the origin of this deviation? The most plausible explanation is that the gas fraction is overestimated because of erroneous labelling of water parts of the signal as bubbly spikes. This is supported by the finding that the gas fraction estimate obtained from the hot-film signal is changed from 5.5 % to 10 % when the threshold used in the threshold method for bubbly-spike detection is changed from $-31.2\ \mathrm{Vs^{-1}}$ to $-21.6\,\mathrm{Vs^{-1}}$ for a flow with a gas fraction of 1.5 % and $Re = 9 \times 10^4$. However, further (smaller) effects may contribute. (i) Errors in the precise estimate of the residence times of the bubbles on the probe may bias the gas fraction estimate as well. (ii) The size of the hot-film probe is finite (typically the order of the size of the bubbles) and not pointwise. To obtain the local gas fraction from a time series, a point measurement tool would be required. It may be expected that the gas fraction measured by a hot-film with a length l is overestimated by a factor of the order of $1 + l/\langle R_b \rangle$, where $\langle R_b \rangle$ is the mean bubble radius. However, as of our case $l/\langle R_b \rangle \approx 0.5$, this effect cannot explain the factor of 4. (iii) The gas volume percentage measured by the U-tube is a global parameter, while the gas fraction measured by the hot-film

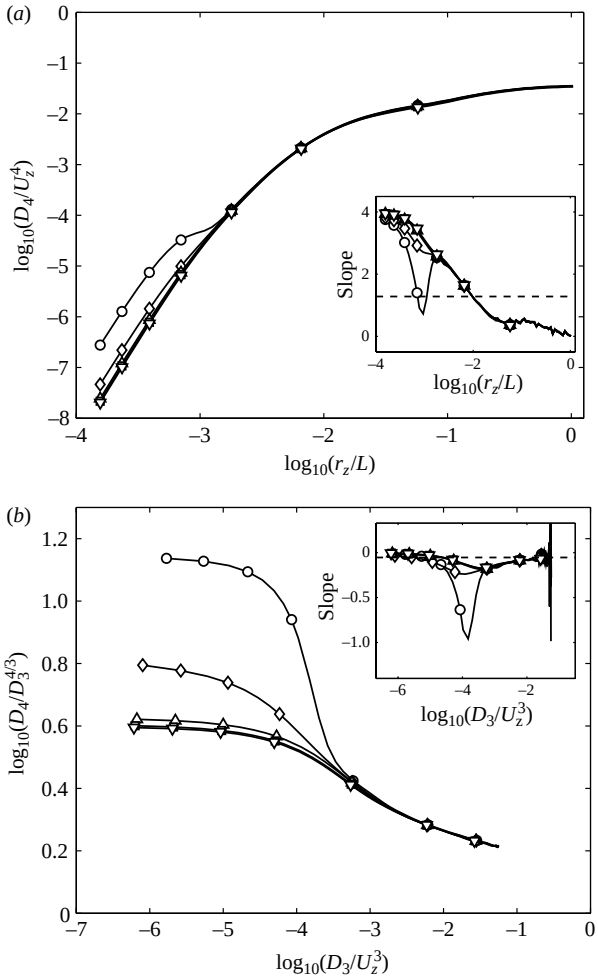

FIGURE 11. Results for a flow with $\alpha = 1.5\,\%$ and $Re \approx 9 \times 10^4$ in the case where the time buffers around the detected bubbles have a length of 0 s (circles), 1.7×10^{-3} s (diamonds), 4.2×10^{-3} s (triangles up), 8.3×10^{-3} s (squares), and 1.7×10^{-2} s (triangles down). (*a*) Plot of D_4/U_z^4 *vs.* r_z/L and its local slope (inset). The dashed line corresponds to a slope of 1.28. (*b*) Plot of $D_4/D_3^{4/3}$ *vs.* D_3/U_z^3 and its local slope (inset). The dashed line corresponds to a slope of -0.05.

probe is a local one. It may be that the difference between those two gas fractions contributes to the overestimate as well. Again, this effect cannot explain the factor of 4 difference. Indeed, an independent measurement of the gas fraction in the centre of the tunnel with an *optical-probe* gave only deviations of the order of 10 % from the results with the U-tube.

To mark the data points that belong to bubbly spikes, it is convenient to have a phase-indication function as described in Bruun (1995). The phase indication vector $\xi = \{\xi_i\}_{i=1}^N$ is defined such that

$$\xi_i = \begin{cases} 1 & \text{fluid}, \\ 0 & \text{bubbly spike}, \end{cases} \tag{3.2}$$

where N denotes the total number of samples of the time series.

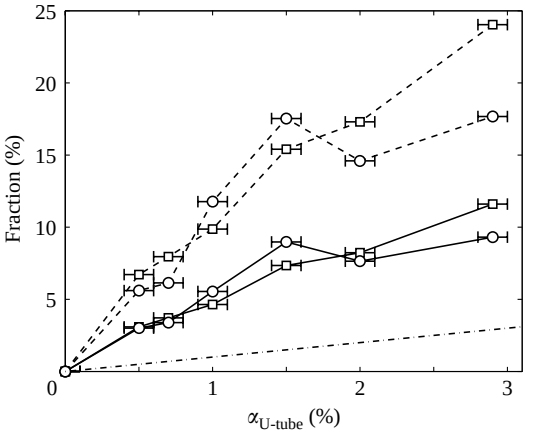

FIGURE 12. Plot of the gas fraction (solid lines) and the dead-time fraction of the signal (dashed lines) obtained from the hot-film signal by the threshold method (squares) and the pattern recognition (circles) *vs.* the gas fraction, α, measured by the U-tube. The dashed-dotted line corresponds to $fraction = \alpha_{U\text{-}tube}$.

3.3.5. *Influence of non-detected bubbly spikes*

As neither bubbly-spike detection methods detect all bubbly spikes, it is important to investigate the effect of non-detected bubbly spikes on the final results. For this purpose, some of the bubbly spikes detected by the threshold method were labelled as water fluctuations. The effect of these spikes on the results can be seen in figures 13 and 14. The figure shows that leaving a fraction of less than 10 % of the bubbly spikes in the signal hardly affects the second-order structure function and the PSD function. In contrast, it has an effect on the fourth-order structure function and on the ESS plots, i.e. leaving only 2 % of the detected bubbles in the signal already gives rather different results.

When all bubbly spikes are left in the signal, the second-order structure function and the PSD function are also affected. Figure 14 shows that in this case a scaling exponent close to $-8/3$ is obtained in the PSD function. It is curious that this number is so close to the power law found by Lance & Bataille (1991). We have no reason to believe that Lance & Bataille (1991) did not carry out the bubble threshold method properly. It may well be coincidence that these numbers are so close.

From figure 13(c, d), we also have to conclude that, in ESS plots, bubbly spikes in structure functions, of different order do not cancel out, as one may have hoped. The reason is that the bubbly spikes have a much larger impact on higher-order structure functions than on lower-order ones.

Though we know that both algorithms used in this study leave some bubbly spikes undetected, it is our belief that there are no better bubbly-spike-detection algorithms available at the moment. We realize that some of the results, especially the higher-order structure functions and the ESS plots, may be influenced by bubbly spikes in the signal. Nevertheless, we are able to show robust results at least for the second-order structure functions and the PSD function, as these results are not very sensitive to some remaining bubbly spikes.

3.4. *Structure functions, ESS and PDFs*

In this subsection, we show how we processed the gapped data to obtain structure functions. The calculation of PDFs and ESS plots was performed in the same way.

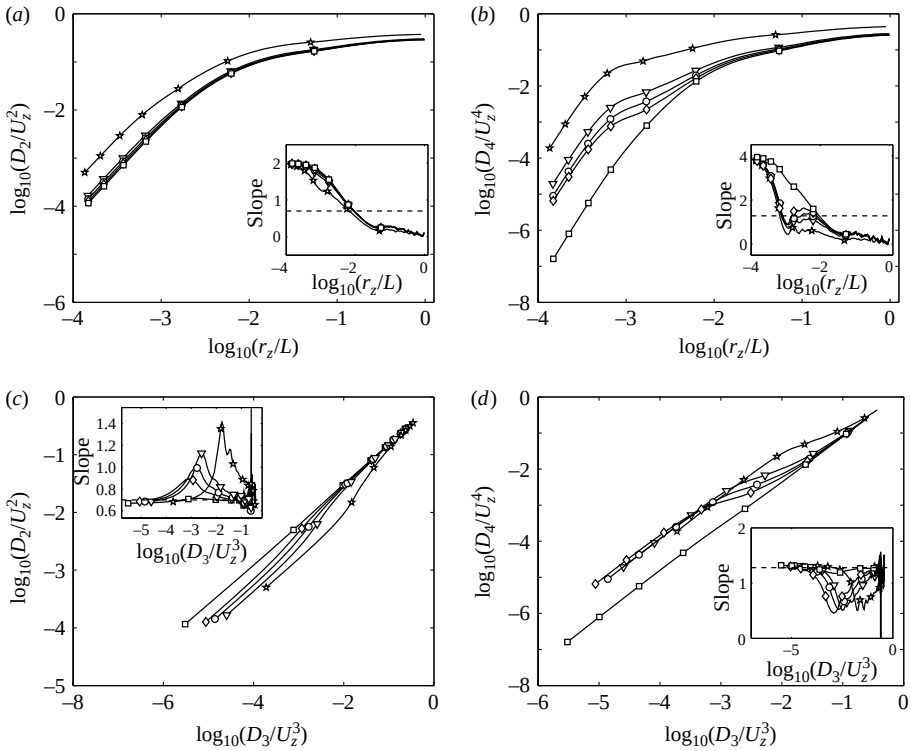

FIGURE 13. Results for a flow with $\alpha = 2.9\,\%$ and $Re = 9 \times 10^4$ in case that 0 % (squares), 2 % (diamonds), 5 % (circles), 10 % (triangles), and 100 % (pentagrams) of the found bubbly spikes were left in the signal. In other words, 100 % (squares), 98 % (diamonds), 95 % (circles), 90 % (triangles), and 0 % (pentagrams) of the detected bubbly spikes were eliminated from the signal through the mask function ξ, equation (3.2). (*a*) Plot of D_2/U_z^2 *vs.* r_z/L. (*b*) Plot of D_4/U_z^4 *vs.* r_z/L. (*c*) Plot of D_2/U_z^2 *vs.* D_3/U_z^3 and its slope (inset). The dashed line corresponds to a slope of 0.7. (*d*) Plot of D_4/U_z^4 *vs.* D_3/U_z^3 and its slope (inset). The dashed line corresponds to a slope of 1.28.

The *pth*-order longitudinal structure function of the velocity is

$$D_p(r_z) = \langle |(u_z(\boldsymbol{x} + r_z, t) - u_z(\boldsymbol{x}, t)|^p \rangle, \tag{3.3}$$

where $u_z(\boldsymbol{x}, t)$ is the local vertical water velocity at a point in space $\boldsymbol{x}$ at time t. Measurements at different instances in time were converted to measurements at different spatial positions using Taylor's hypothesis, $r_z = U_z \cdot \tau$, where τ is the time difference between samples that are compared and U_z the mean downward velocity of the water flow.

Using the notation of (3.2) and Taylor's hypothesis, the structure function of a bubbly flow signal can be obtained by

$$D_p(r_z = U_z\tau) = \frac{\displaystyle\sum_{i=1}^{N-\tau} \xi_i \xi_{i+\tau} |u_{z,i} - u_{z,i+\tau}|^p}{\displaystyle\sum_{i=1}^{N-\tau} \xi_i \xi_{i+\tau}}. \tag{3.4}$$

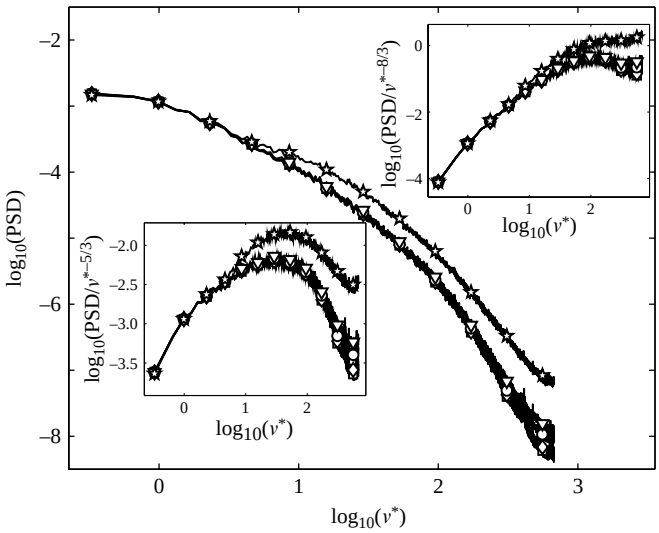

FIGURE 14. PSD, PSD divided by $\nu^{*-5/3}$ (left-hand inset), and PSD divided by $\nu^{*-8/3}$ (right-hand inset) *vs.* the dimensionless frequency $\nu^* = \nu U/L$ for a flow with $\alpha = 2.9\,\%$ and $Re = 9 \times 10^4$ in the case where 100 % (squares), 98 % (diamonds), 95 % (circles), 90 % (triangles), and 0 % (pentagrams) of the found bubbly spikes were eliminated from the signal. The upper inset clearly shows that a $-8/3$ power law is obtained once all bubbly spikes are left in the signal.

The robustness of (3.4) is validated using test data. The test data are obtained by taking a single-phase flow signal and gapping it artificially. We used the phase indication function of a two-phase flow signal to gap the single-phase flow signal in a realistic way. In figure 15, we can see the resulting fourth-order structure function and the fourth-order compensated ESS plot. The figure shows that taking out parts of the single-phase flow hardly affects the structure function, nor the ESS plot. (Note the extremely well resolved scales of the left insets.) Therefore, we conclude that the effect of the gapping is negligible for the structure functions and the ESS plots. It is obvious that the same holds for the PDFs.

3.5. *Power spectra*

The standard method for obtaining spectra from continuous time series is the Welch method (Welch 1967). Here, however, we have incomplete time series and Welch's method has to be modified. We fill the bubbly gaps by means of linear interpolation and apply Welch's average periodogram. The results obtained for the test data (see § 3.4) can be seen in figure 16(*a*).

Although the results of this test seem to be satisfactory at first sight, filling the gaps by means of linear interpolation has some influence on the results. That influence is highlighted in the insets of figure 16(*a*), which show the compensated spectrum and the ratio of the complete spectrum and the gapped spectrum. It can be seen that the gapping has a *selective* effect on the spectrum *at higher frequencies*, so that the slope of the spectrum becomes modified. For an analysis focusing on the scale-resolved effect of bubbles on turbulence, this shortcoming of the method is clearly not acceptable.

Consequently, a second method must be applied to estimate the spectra. This second method is an autoregressive time series model. A simple autoregressive model expresses the time series $u_z(t)$ as a linear combination of the value of a white noise

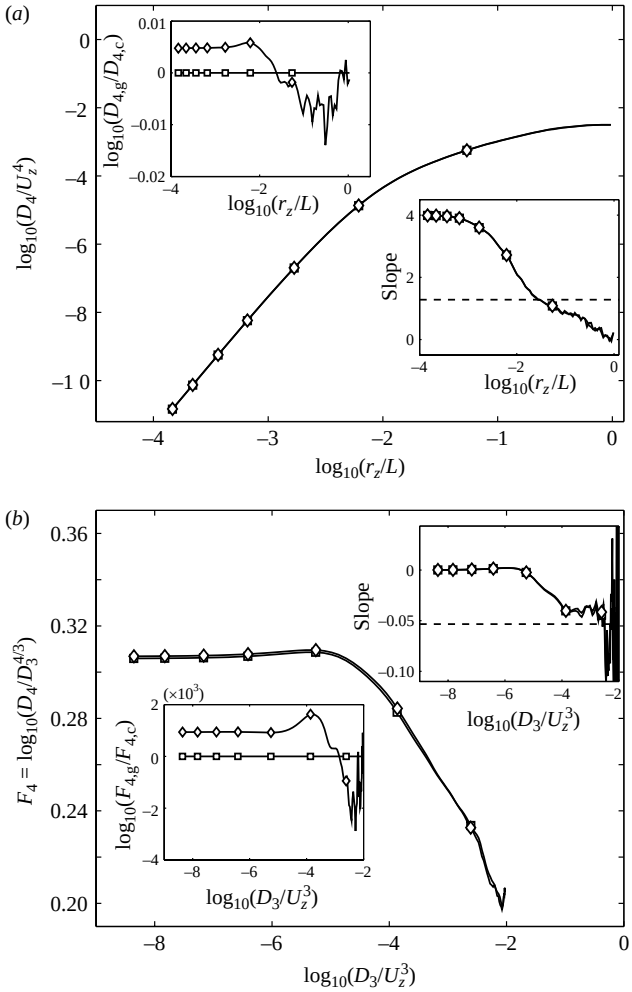

FIGURE 15. Results of a single-phase flow with $Re = 9 \times 10^4$ in the case of processing a complete time series (squares) and a time series that was artificially gapped (diamonds). To gap the data the phase indication function of a two-phase flow signal with a gas fraction of $\alpha = 2.9\,\%$ was used. (*a*) Plot of D_4/U_z^4 *vs.* r_z/L and its local slope (right-hand inset). The dashed line corresponds to a slope of 1.28. (*b*) Compensated ESS plot of $F_4 = D_4/D_3^{4/3}$ *vs.* D_3/U_z^3 and its local slope (right-hand inset). The dashed line corresponds to a slope of -0.05. The left insets show the ratio of the results for the gapped and the complete signal. Note the well-resolved scale of the *y*-axes of the left-hand insets; the structure functions for the complete and for the gapped signal basically agree.

process $\epsilon(t)$ and a finite number of lagged values of the time series. The nth-order autoregressive process, AR(n), is defined by

$$u_z(t) + \alpha_1 u_z(t-1) + \cdots + \alpha_n u_z(t-n) = \epsilon(t), \tag{3.5}$$

where α_1 to α_n are the parameters of the model.

To find the parameters α_k we applied the Matlab ARX routine that uses the least-squares method without windowing, also known as the covariance method. Once the parameters of the model are known, the spectra can be obtained. For more details on AR-modelling, refer to Ljung (1999).

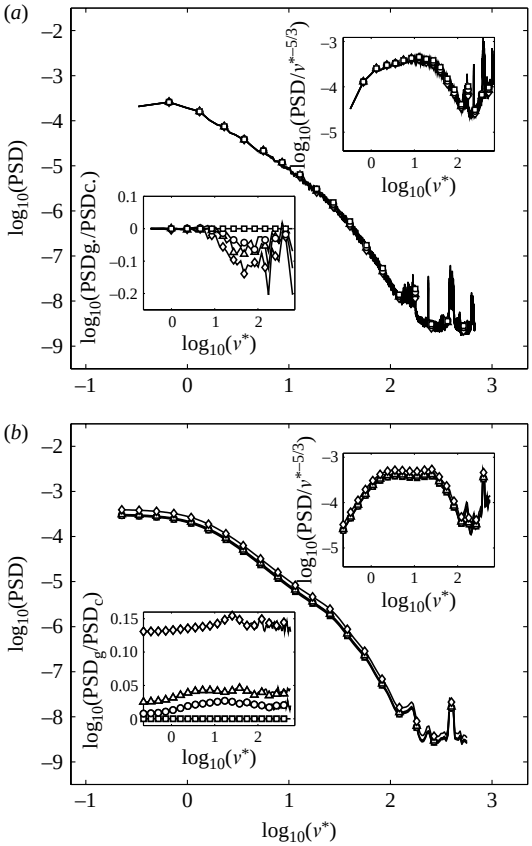

FIGURE 16. Results of processing the complete single-phase data (squares) and data that were artificially gapped. To gap the data, phase indication functions of two-phase flow with gas fractions of $\alpha = 1.0\,\%$ (circles), $\alpha = 2.0\,\%$ (triangles), and $\alpha = 2.9\,\%$ (diamonds) were used. (*a*) Power spectral density function obtained by the Welch's averaged periodogram method. In the right-hand inset the compensated spectrum is shown. The window length was 2^{12} samples, the overlap of the windows was 2^{11} samples, and no windowing function was used. The left insets show the ratio of the results for the gapped and the complete signal. Both insets clearly show that there is a frequency drift in the performance of the Welch algorithm for gapped data, so that the slope of the spectrum becomes modified. (*b*) Power spectral density function obtained by AR(40)-modelling. In the right-hand inset the compensated spectrum is shown. The left-hand insets show the ratio of the results for the gapped and the complete signal. Both insets demonstrate that there is no frequency drift with this method, and slopes therefore remain unchanged, therefore making this method the method of choice for our application. The time series under consideration has a length of 20 min and is of a single-phase flow with $Re = 9 \times 10^4$.

First, we show that for a *continuous* signal the ARX routine is as powerful as the Welch model. Figure 17 demonstrates that there is good agreement between the AR-model and Welch's average periodogram. Note that the AR method suppresses the noisy peaks present in the PSD.

Next we come to the gapped signals. In order to deal with the gaps, we used multiple-experiment modelling, i.e. the time-intervals between successive bubble–probe interactions were considered as separate experiments. The parameters of the model were estimated using all separate experiments simultaneously. The multi-experiment

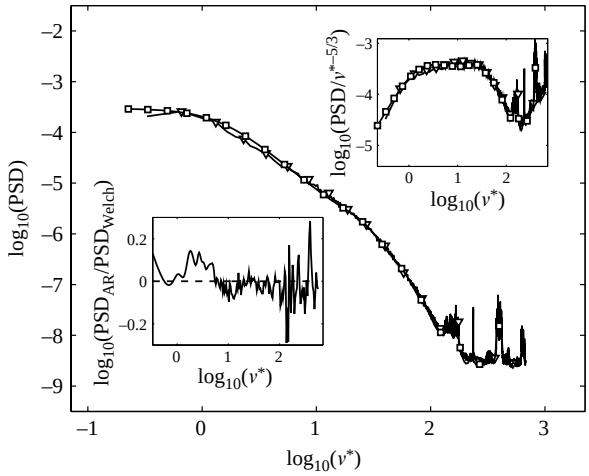

FIGURE 17. PSDs for a continuous times series, in order to demonstrate that in that case the Welch's averaged periodogram (triangles) method and the AR(40)-model (squares) give the same results. The right-hand inset shows the compensated spectrum. The left-hand inset shows the ratio of the PSD estimate of Welch's averaged periodogram and the AR(40) model. The signal under consideration is a hot-film anemometer velocity signal of 20 min of a single-phase flow with $Re = 9 \times 10^4$.

AR modelling is applied to the test data. The results are shown in figure 16(*b*). The figure shows good agreement between the results of the gapped and the non-gapped signal, when the phase indication function used belonged to a two-phase flow signal with a gas fraction of $\alpha \leqslant 2.0\,\%$. The result for the gapped signal deviates very slightly from the result for the non-gapped signal, when a phase indication function of a two-phase flow with a gas fraction of $\alpha = 2.9\,\%$ was used, but no selective drift in a certain frequency domain as in the Welch method is seen. The interarrival time between bubbles becomes shorter in the case of higher gas fractions. An AR(n) model requires the length of the segments to be at least $(n-1)/2$ samples. No segments that are shorter will be used for the modelling. As a consequence, the performance of the algorithm becomes worse for high gas fractions. We conclude that the AR-method gives a good estimate of the PSD of gapped data up to a gas fraction of $\alpha = 2.0\,\%$. In particular, no frequency drift occurs as with the Welch method.

4. Results

4.1. *PDF*

The most direct tool for investigating the intermittency is to look at the PDFs of the velocity increment $\Delta U_z(r_z)$. When intermittency is present, the PDFs evolve from a Gaussian distribution for large scales towards stretched exponentials for decreasing r_z (e.g. Frisch 1995; Tabeling *et al.* 1996; Pope 2000). To ensure that the standard deviation of the PDFs is equal to 1, we rescale the velocity increments,

$$s = \frac{\Delta U_z(r_z)}{\langle (\Delta U_z(r_z))^2 \rangle^{0.5}}. \tag{4.1}$$

In figures 18 and 19, we can see PDFs of the velocity increments s as defined in (4.1) for two different gas fractions $\alpha = 1.5\,\%$ and $\alpha = 2.9\,\%$ and different distances r_z for the case where the bubbly spikes are detected by either the threshold method or the

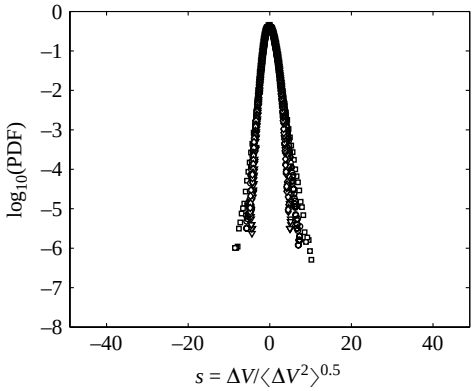

FIGURE 18. PDFs of the velocity increments s for a single-phase flow with $Re \approx 9 \times 10^4$ on the scales $r_z \approx 8\eta$ (squares), $r_z \approx 64\eta$ (circles), $r_z \approx 512\eta$ (triangles) and $r_z = L = 4500\eta$ (diamonds). The chosen scale on the s-axis is the same as in the next figure to allow for a comparison between single- and two-phase flow.

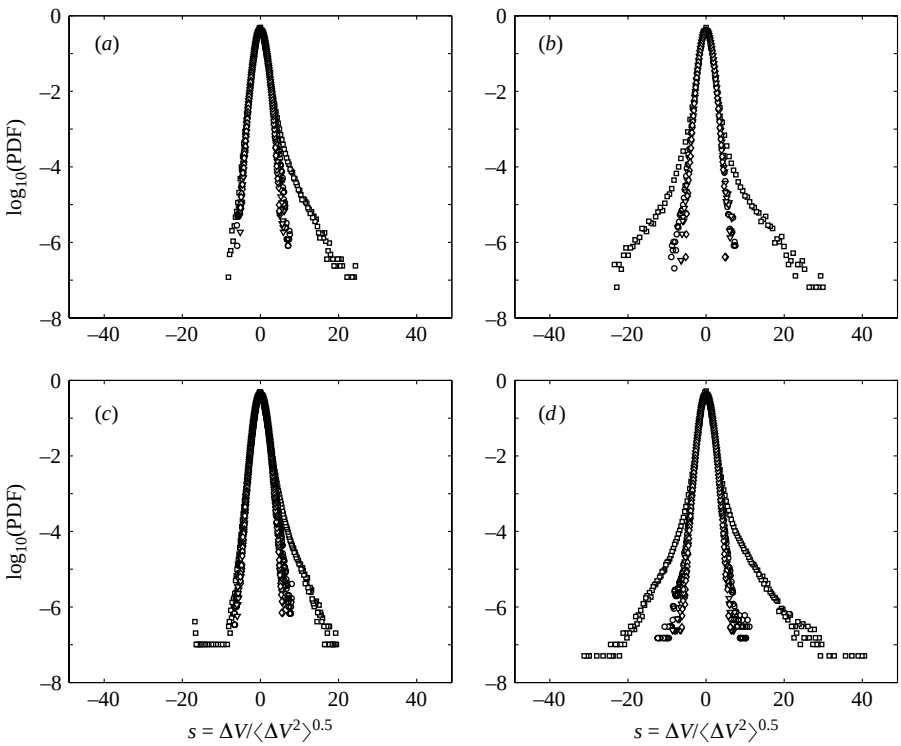

FIGURE 19. PDFs of the velocity increments s for flow with $Re \approx 9 \times 10^4$ and (a, b) $\alpha = 1.5\,\%$ and (c, d) $\alpha = 2.9\,\%$ on the scales $r_z \approx 8\eta$ (squares), $r_z \approx 64\eta$ (circles), $r_z \approx 512\eta$ (triangles), and $r_z = L = 4500\eta$ (diamonds). To detect the bubbly spikes in the signal, both (a, c) the threshold method and (b, d) the pattern recognition method were applied.

pattern-recognition method. The corresponding skewnesses and flatnesses are given in table 4. The figures and the table show that PDFs of the different flows are almost identical on large scales $r_z = L$, $r_z \approx 512\eta$ and even $r_z = 60\eta$. On the very small scales, $r_z = 8\eta$, differences can be seen between the single-phase flow and the two-phase flow.

Function	r	Single phase	Threshold method		Pattern recognition	
			$\alpha = 1.5\,\%$	$\alpha = 2.9\,\%$	$\alpha = 1.5\,\%$	$\alpha = 2.9\,\%$
S	8η	1.90	2.10	2.02	2.33	2.42
	64η	1.74	1.73	1.72	1.67	1.70
	512η	1.63	1.65	1.65	1.65	1.65
	$L = 4500\eta$	1.59	1.62	1.61	1.62	1.61
F	8η	4.77	7.01	5.95	10.62	11.42
	64η	3.79	3.73	3.66	3.41	3.58
	512η	3.16	3.29	3.27	3.28	3.29
	$L = 4500\eta$	2.98	3.11	3.07	3.10	3.08

TABLE 4. Skewness S and flatness F of the various PDFs shown in figures 18–19.

The PDFs of the two-phase flows show an increase of the intermittency on the small scales compared to the single-phase flow. The increase is comparable for the two different gas fractions under consideration. This finding is remarkable, as it suggests that already a relatively small fraction is sufficient to change the statistical properties of the flow, and adding extra bubbles does not have a large effect. We will find this features again in all structure functions and ESS plots that we will consider later. The lowest gas percentage we analysed was $\alpha = 0.5\,\%$. The transition with respect to the statistical properties of bubbly flow as compared to single-phase flow therefore already seems to happen for bubble concentrations lower than 0.5 %.

This finding also suggests that undetected bubbly spikes, indeed, are not a major problem. If so, there would be a drift in the statistical properties of the signal with increasing bubble concentration, as, of course, more bubbles would mean a larger probability of undetected spikes.

At the very small scales, $r_z = 8\eta$, the changes are not equal for the two bubbly-spike detection methods. With the present data material and detection techniques there is no way of saying which method would be the more correct one. As already shown in the validation section (§ 3.3.3), the two different methods identify different parts of the signal as bubbly spikes, though the overlap is, of course, considerable.

We think that the asymmetry in the PDFs obtained by applying the threshold method is introduced by the threshold method itself. The threshold method detects bubbly spikes using a threshold on the *negative* derivative of the signal. In § 3.3.3, we showed that the method labels some water parts as bubbly spikes. These water parts contain a relatively large decrease of the water velocity. The misclassification of those signal parts is probably causing the asymmetry, as these water parts are filtered out from the signal while those with a relative large increase of the water velocity are left in the signal. This explanation of the asymmetry is supported by the finding that the asymmetry is the other way round when a *positive* threshold on the derivative of the hot-film signal is used to detect the bubbly spikes.

4.2. *Structure functions*

In figures 20 and 21, the second- and fourth-order structure functions and their local slopes can be seen for the case when the bubbly spikes are detected by either the threshold method or the pattern-recognition method. The results for the second-order structure function are similar for both methods. Both figures show an increase of the energy for increasing gas fractions. This increase of the energy is non-uniform, i.e. it is more pronounced on small scales than on large scales. Correspondingly, the slope is

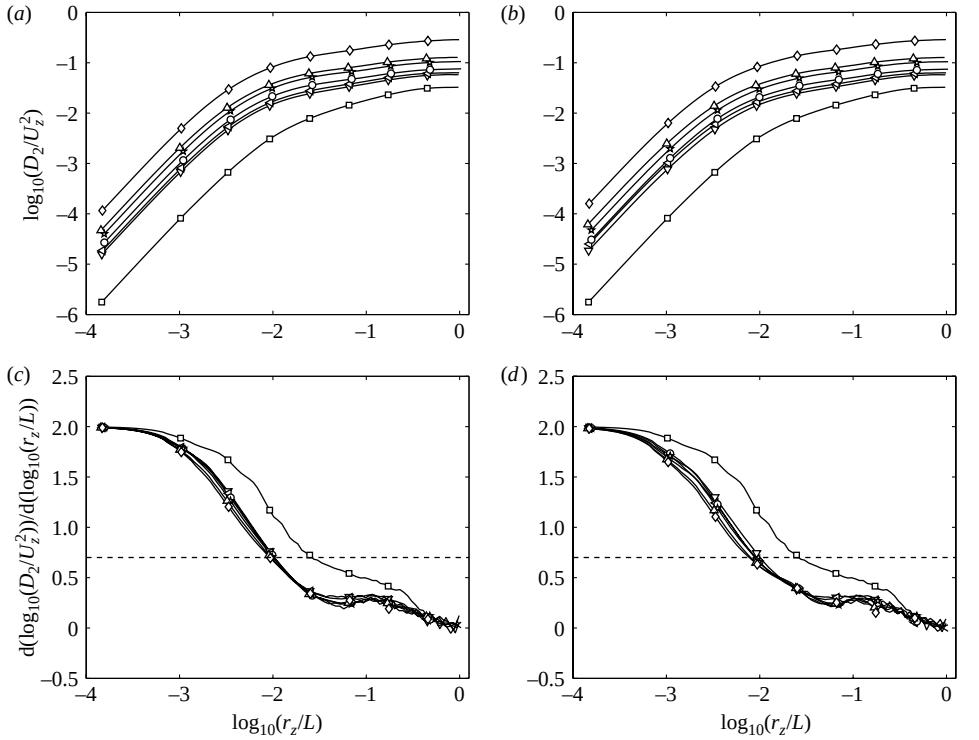

FIGURE 20. (a, b) Second-order structure functions and (c, d) their slopes for flow with $Re \approx 9 \times 10^4$ and gas fractions of $\alpha = 0\,\%$ (squares), $\alpha = 0.5\,\%$ (triangles down), $\alpha = 0.7\,\%$ (triangles left), $\alpha = 1.0\,\%$ (circles), $\alpha = 1.5\,\%$ (pentagrams), $\alpha = 2.0\,\%$ (triangles up), and $\alpha = 2.9\,\%$ (diamonds). The dashed lines correspond to a slope of 0.7. To detect the bubbly spikes in the signal, both (a, c) the threshold method and (b, d) the pattern recognition method were applied.

reduced. This finding corresponds qualitatively with the numerical results of Mazzitelli *et al.* (2003*a*, *b*). It is consistent with our findings on the PDFs, too, which also show more activity on small scales, whereas the large scales remain unchanged. We again note, as already in section 1, that there are differences between experiments and numerics: Obviously, the bubbles in experiment are not point-wise, as model in the numerics of Mazzitelli *et al.* (2003*a*, *b*), but have an extension of on average of several Kolmogorov scales η, thus showing vortex shedding and even shape oscillations. All these effects could have an influence on the results which is not considered in the numerics. However, as the typical bubble radius is about 10–20η and thus not too far from the the viscous subrange (VSR), from our point of view, the dominant effect of the bubble remains a rather localized forcing due to the bubble's buoyancy.

One difference with the numerical simulation of Mazzitelli *et al.* (2003*a*, *b*) is that here we do not see a decrease of the energy on large scales as found in those papers. An origin of this difference may be that in contrast to the numerical simulations, here we fixed the velocity of the different flow and not the total energy. Owing to gas lift, more energy is required to preserve the same water velocity in our two-phase flow.

Figure 20 shows that the gas fraction does not seem to have a large influence on the value of the slope. Once the gas fraction is beyond $\alpha = 0.5\,\%$, the slope remains unchanged, just as the PDFs did. Unfortunately, we do not have any measurements between $\alpha = 0$ and 0.5 %, to study the transition from single-phase to two-phase flow.

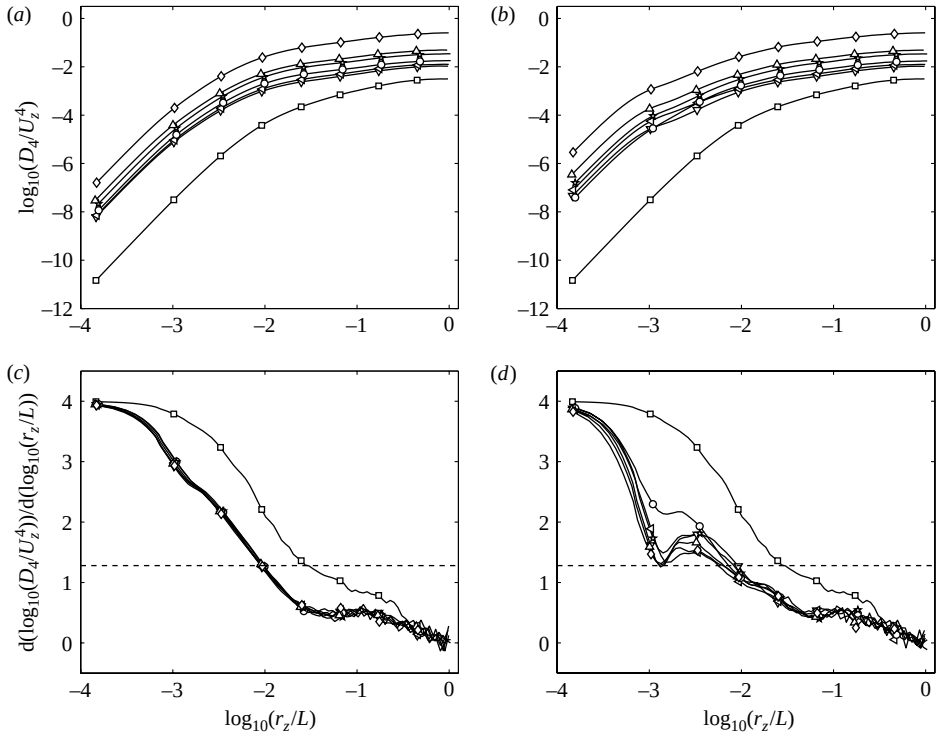

FIGURE 21. (a, b) Fourth-order structure functions and (c, d) their slopes for flow with $Re \approx 9 \times 10^4$ and gas fractions of $\alpha = 0\,\%$ (squares), $\alpha = 0.5\,\%$ (triangles down), $\alpha = 0.7\,\%$ (triangles left), $\alpha = 1.0\,\%$ (circles), $\alpha = 1.5\,\%$ (pentagrams), $\alpha = 2.0\,\%$ (triangles up), and $\alpha = 2.9\,\%$ (diamonds). The dashed lines correspond to a slope of 1.28. To detect the bubbly spikes in the signal, both (a, c) the threshold method and (b, d) the pattern-recognition method were applied.

The results for the fourth-order structure function (figure 21) shows the same behaviour as the second-order structure function, i.e. a non-uniform increase of the energy and the same slope for all two-phase flow cases. However, on small scales, some differences can be seen between the two bubbly-spike detection methods. Both figures also show a change in the slope at $r_z/L \approx 10^{-3}$. This change is due to the application of the low-pass filter with a cut-off at 300 Hz which corresponds to $r_z/L \approx 10^{-3}$. The minimum in the local slope of $\log_{10}(D_4(r)/U_z^4)$ obtained with the pattern-recognition method, see figure 21, seems to be an artefact to us; we have no explanation for that.

4.3. *ESS*

Structure functions of flow with a low Reynolds number often do not show any scaling with the space variable r_z. However, Benzi *et al.* (1993), Briscolini *et al.* (1994) and many others have shown that even in the case of low Reynolds number, the flow can have pronounced scaling properties, namely when plotting structure functions of order p *vs.* the third-order structure function rather than *vs.* the space variable r_z. This property is called extended self-similarity (ESS). Using extended self-similarity plots, scaling can be found over a much wider range than for the situation where the structure functions are plotted versus the scale variable r_z, but not below 10η. Usually, $\langle|\Delta U_z(r_z)|^3\rangle$ instead of $|\langle\Delta U_z(r_z)^3\rangle|$ is used in ESS plots, because of the poor statistical convergence of $|\langle\Delta U_z(r_z)^3\rangle|$, and we do so, too.

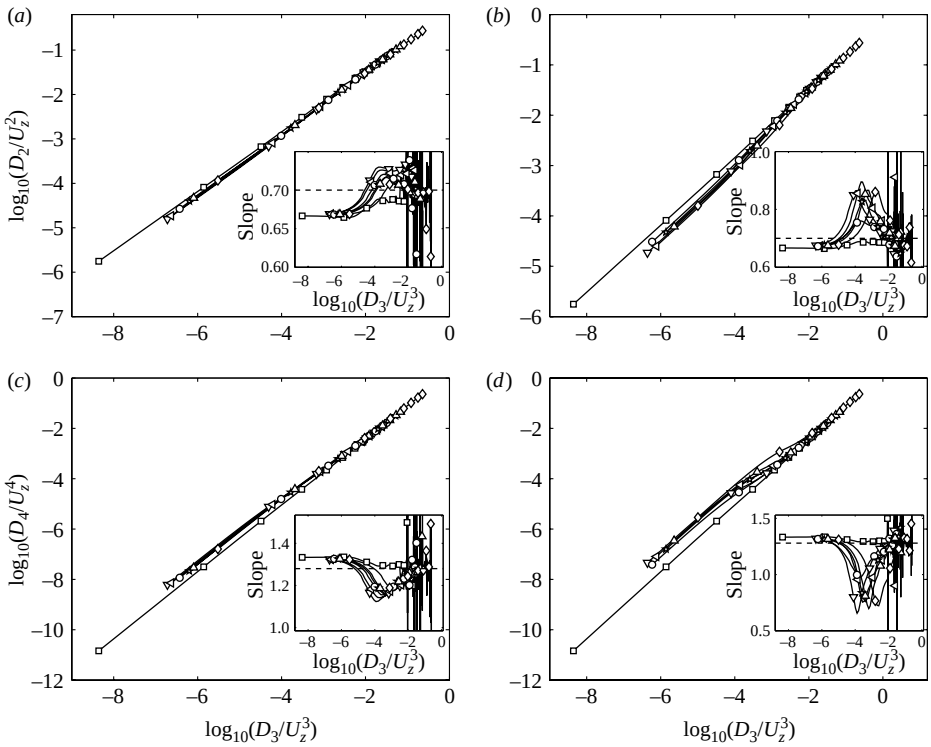

FIGURE 22. (a, b) ESS plots of the second-order structure functions and (c, d) the fourth-order structure function and their slopes (insets) for flow with $Re \approx 9 \times 10^4$ and gas fractions of $\alpha = 0\,\%$ (squares), $\alpha = 0.5\,\%$ (triangles down), $\alpha = 0.7\,\%$ (triangles left), $\alpha = 1.0\,\%$ (circles), $\alpha = 1.5\,\%$ (pentagrams), $\alpha = 2.0\,\%$ (triangles up), and $\alpha = 2.9\,\%$ (diamonds). The dashed lines in the upper plots correspond to a slope of 0.7 and those in the lower plots correspond to a slope of 1.28. To detect the bubbly spikes in the signal both (a, c) the threshold method and (b, d) the pattern-recognition method were applied.

In figure 22, we compare the second- and fourth-order ESS plots for single-phase and two-phase flow. For single-phase flow, we recover the well-known scaling ESS exponents 0.70 and 1.28 in the ISR and in the large scale range, see e.g. Arneodo *et al.* (1996) or Briscolini *et al.* (1994), Frisch (1995), Grossmann *et al.* (1997*b*). In the case of two-phase flow, this very scaling is found on the largest scales, but is lost towards smaller scales, with even quantitatively similar deviations within both bubble-detection schemes. Thus, the extended self-similarity property is destroyed in bubbly flow. This result is consistent with our earlier findings on the PDFs and the structure function itself. Indeed, it is intuitive that the ESS property is lost once rising bubbles force the turbulence on smaller scales. Note, however, that another buoyancy-driven turbulence, namely thermally driven turbulence, still enjoys the property of extended self-similarity, though with different scaling exponents (Benzi *et al.* 1996).

The results for the fourth-order ESS plots show the same trend as the second-order ESS plots. Again, the standard slope 1.28 survives only on the largest scales, but is lost on smaller ISR scales, with little difference between the cases with different bubble concentration. The deviation between the results of the two different bubbly-spike detection methods is again slightly larger in the fourth-order moments than in the second-order moments.

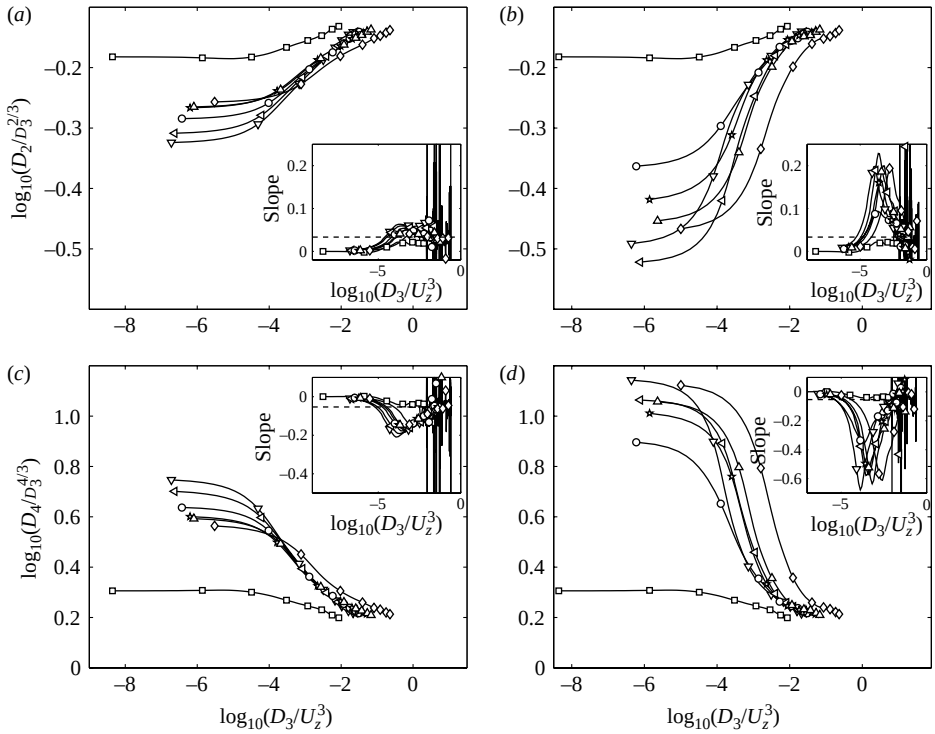

FIGURE 23. (a, b) Compensated ESS plots of the second-order structure functions and (c, d) the fourth-order structure function for flow with $Re \approx 9 \times 10^4$ and gas fractions of $\alpha = 0\,\%$ (squares), $\alpha = 0.5\,\%$ (triangles down), $\alpha = 0.7\,\%$ (triangles left), $\alpha = 1.0\,\%$ (circles), $\alpha = 1.5\,\%$ (pentagrams), $\alpha = 2.0\,\%$ (triangles up), and $\alpha = 2.9\,\%$ (diamonds). The dashed lines correspond to (a, b) intermittency corrections of 0.03 and (c, d) -0.05. To detect the bubbly spikes in the signal both (a, c) the threshold method and (b, d) the pattern-recognition method were applied.

For better visualization of the intermittency effects in ESS plots, Grossmann *et al.* (1997*a*) have employed *compensated* ESS plots. In figure 23, we replot the data of figure 22 in this compensated way, which reveals better the stronger intermittency properties on the smaller scales for the two-fluid case. Again, this is consistent with what we found for the PDFs and the structure functions itself.

4.4. *Spectra*

We now come to the effect of the bubbles on the spectra. Though the spectrum, in principle, contains the same information as the second-order structure function, in practice, the transformation from one to the other is non-trivial, and finite size effects are important (Lohse & Müller-Groeling 1995, 1996). As spectra are the most common way to represent the effect of bubbles on developed turbulence, we also give them here.

In figure 24, the power spectra density plots as obtained by Welch's averaged periodogram method can be seen for the case where the bubbly spikes are detected by either the threshold method or the pattern-recognition method. Figure 25 shows the same as figure 24, but in that figure the power spectral density is obtained by the auto-regressive modelling, which in § 3 we had judged to be the more reliable method, as spectra of gapped time series do not suffer from frequency dependent drifts.

For single-phase flow, the spectra show the Kolmogorov $-5/3$ scaling, including a small bottleneck effect at the transition between ISR to VSR (Falkovich 1994;

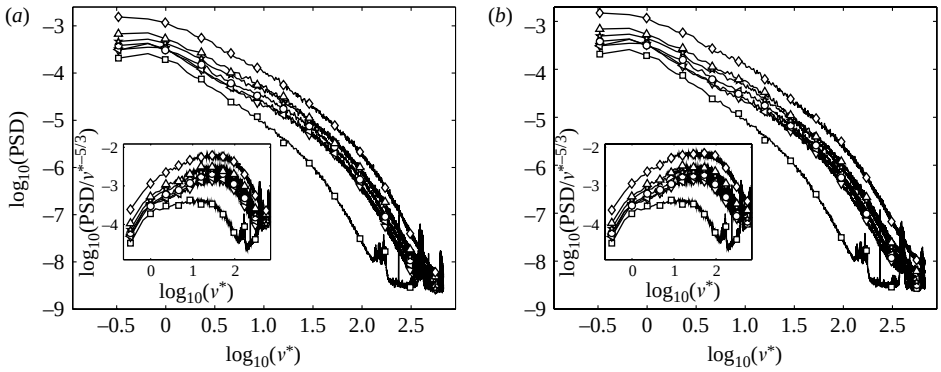

FIGURE 24. Power spectral density plots and compensated power spectral density plots (insets) as obtained by Welch's averaged periodogram method for flow with $Re \approx 9 \times 10^4$ and gas fractions of $\alpha = 0\,\%$ (squares), $\alpha = 0.5\,\%$ (triangles down), $\alpha = 0.7\,\%$ (triangles left), $\alpha = 1.0\,\%$ (circles), $\alpha = 1.5\,\%$ (pentagrams), $\alpha = 2.0\,\%$ (triangles up), and $\alpha = 2.9\,\%$ (diamonds), for the case where the bubbly-spike detection was performed by (*a*) the threshold method and (*b*) by the pattern recognition.

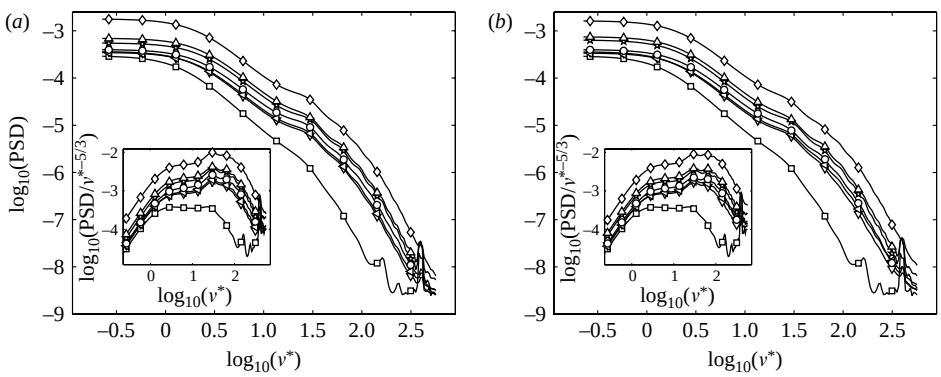

FIGURE 25. Power spectral density plots and compensated power spectral density plots (insets) as obtained by auto-regressive modelling for flow with $Re \approx 9 \times 10^4$ and gas fractions of $\alpha = 0\,\%$ (squares), $\alpha = 0.5\,\%$ (triangles down), $\alpha = 0.7\,\%$ (triangles left), $\alpha = 1.0\,\%$ (circles), $\alpha = 1.5\,\%$ (pentagrams), $\alpha = 2.0\,\%$ (triangles up), and $\alpha = 2.9\,\%$ (diamonds), for the case where the bubbly-spike detection was performed by (*a*) the threshold method and (*b*) by the pattern recognition.

Lohse & Müller-Groeling 1995). As is well known, intermittency effects are not very visible in spectra.

For the two-phase flow, we measure a strong spectral energy increase at large frequencies (corresponding to small scales) and a mild spectral energy increase at small frequencies (corresponding to large scales), leading to a less steep slope as compared to $-5/3$. This finding is in accordance to the above findings on the second-order structure function, where we also found a large increase on small scales and a small increase on large scales, see figure 20.

Our experimental finding on the spectra resembles the numerical finding on the effect of two-way coupled point-bubbles of Mazzitelli *et al.* (2003*a*, *b*), where a strong increase on small scales and thus a reduced slope was found, too. However, in those numerical simulations also a spectral energy decrease was detected at large scales.

The reason for this difference between experiment and numerics is that in the former case the flow velocity was kept constant, whereas in the latter case the energy input (excluding the input by the bubbles) was kept constant.

The two-phase flow spectra again show the feature (as the PDFs, structure functions and ESS plots) that the largest transition is between the single-flow case $\alpha = 0\,\%$ and $\alpha = 0.5\,\%$, whereas adding further bubbles shifts the spectra only slightly further up.

5. Conclusions

The influence of bubbles on a fully developed turbulent flow has been investigated by performing hot-film anemometry measurements in the Twente water tunnel. We used gas fractions of 0.5 % up to 2.9 % and a Reynolds number of 9×10^4. We obtained probability distribution functions, structure functions, extended self-similarity (ESS) functions, compensated ESS functions, and power spectra of the water velocity time series.

Our results for both the structure functions and the power spectral density functions show an increase of the energy for two-phase flow compared to single-phase flow, which is more pronounced on small scales than on large scales. This corresponds qualitatively with the results of Mazzitelli *et al.* (2003*a*). This result proved to be robust for different signal-processing methods and misdetections of a few per cent of the disturbances in the hot-film signal that are caused by the sudden change of the heat transfer when a bubble touches the hot film. We did not observe a progressive substitution of the scaling exponent of $-5/3$ by a scaling exponent of $-8/3$ in the power spectral density functions for increasing gas fractions as found by Lance & Bataille (1991). This may be rationalized by the different bubblance parameter b in the present work and the work of Lance & Bataille (1991). In the latter work, the slope of $-8/3$ is only found when the energy associated to the perturbations of the liquid is dominated by pseudoturbulence, i.e. large $b > 1$, whereas here we have $b < 1$. The reason for the large bubblance parameter b in the measurements of Lance & Bataille (1991) is that these authors use relatively large bubbles and weak turbulence. However, as illustrated by table 1, associating a spectral slope $-5/3$ with a regime with $b < 1$ and a slope $-8/3$ with a regime $b > 1$ is too simplistic; there are various experiments and numerical simulations with $b = \infty$ and a spectral slope close to $-5/3$ nevertheless.

A possible solution to the discrepancy between the $-5/3$ and $-8/3$ scaling might be different properties of the near field directly in the wake behind the bubble and the far field away from the bubbles. (For visualizations of the wake see e.g. Brücker 1999; de Vries *et al.* 2002; Lima-Ochoterena & Zenit 2003; Veldhuis *et al.* 2005.) The results of Larue de Tournemine (2001) and Cartellier & Rivière (2001) are consistent with this interpretation. The idea here would be that in-spite of the small dead time our signal, processing method could cut out part of the near field caused by the wake immediately behind the bubble, which may be responsible for the $-8/3$ scaling. Whether this is indeed the case can only be answered by future experiments.

From a qualitative point of view, i.e. not focusing on scaling exponents but on the frequency-dependent modifications of the spectrum, the results of Lance & Bataille (1991), the experimental results here or the numerical results of Mazzitelli *et al.* (2003*a*, *b*) are quite similar. When comparing figure 15 of Lance & Bataille (1991) or figure 3 of Mazzitelli *et al.* (2003*b*) with figure 25 here, we find that the bubbles cause a strong energy enhancement on small scales and a small energy reduction at large scales (or only a weak enhancement in the experiments here owing to the

different experimental procedure, namely, holding the flow velocity rather than the energy input constant).

Both the PDFs and the compensated ESS plots show that intermittency is enhanced because of the presence of bubbles. Once bubbles are present in the flow, the dependence on the actual bubble concentration is weak. The ESS plots show that, towards small scales, the extended self-similarity property is destroyed in turbulent bubbly flow.

Finally, we would like to caution the reader. Though we have applied two different bubbly-spike detection methods to find the disturbances caused by bubble–probe interactions in the hot-film signals, and though visual inspection of the results of both methods suggests that only a few per cent of the bubbly spikes were not detected, we cannot check the exact performance of either of the two methods, owing to a lack of more reliable verification methods. Therefore, our results on the ESS plots and the intermittency may be influenced by the presence of some bubbly spikes in the signals. This is supported by the finding of modest differences in the results for the two different bubbly-spike detection methods for higher-order structure functions and intermittency corrections. We, however, hope to have demonstrated that at least qualitatively our results are robust.

How to further improve on bubble detection in turbulent two-phase flow? Our strategy is the following. First, we will try *simultaneous* measurements of hot-probe and optical fibre measurements at the same position. The latter method is known to hardly disturb the flow (Cartellier 1992; Mudde & Saito 2001) and thus allows for an unambiguous detection of the bubbles at the probe. Thus, we will obtain an unbiased training set of bubbly-spike events, with which we plan to 'train' the neural-network type pattern-recognition scheme. The trained scheme can then detect the bubbles in long hot probe time series of the same type in which no extra optical probe has been employed. Obviously, once a hot-probe is stably combined with an optical fibre measurement at the probe position, all bubble-detection schemes will become redundant. Up to that time, the community will have to cope with imperfect measurements.

We thank Michel Lance, Jacques Magnaudet, Rob Mudde, Gijs Ooms, Andrea Prosperetti, Willem van der Water, Jerry Westerweel and Leen van Wijngaarden for their comments and advices and Sebastian Guet and the Delft-group for letting us use their four-point optical probe. We would also like to thank Gert-Wim Bruggert, Hennie Scholten, and Bas Benschop for their continuous technical assistance without which this work would not have been possible. J. R. acknowledges support from FOM. S. L. acknowledges support from the European Union (EU) through the European Research Network on 'Nonideal Turbulence' (contract HPRN-CT-200000162).

REFERENCES

Arneodo, A., Baudet, C., Belin, F., Benzi, R., Castaing, B., Chabaud, B., Chavarria, R., Ciliberto, S., Camussi, R., Chilla, F., Dubrulle, B., Gagne, Y., Hebral, B., Herweijer, J., Marchand, M., Maurer, J., Muzy, J. F., Naert, A., Noullez, A., Peinke, J., Roux, F., Tabeling, P., van de Water, W. & Willaime, H. 1996 Structure functions in turbulence, in various flow configurations, at Reynolds number between 30 and 5000, using extended self-similarity. *Europhys. Lett.* **34**, 411.

Belin, F., Tabeling, P. & Willaime, H. 1996 Exponents of the structure function in a low temperature helium experiment. *Physica* D **93**, 52.

Benzi, R., Biferale, L., Ciliberto, S., Struglia, M. V. & Tripiccione, R. 1996 Generalized scaling in fully developed turbulence. *Physica* D **96**, 162.

Benzi, R., Ciliberto, S., Tripiccione, R., Baudet, C., Massaioli, F. & Succi, S. 1993 Extended self-similarity in turbulent flows. *Phys. Rev.* E **48**, R29–R32.

van den Berg, T. H., Luther, S. & Lohse, D. 2005 The effect of microbubbles on fully developed turbulence: experiments. *Phys. Fluids*. (Submitted).

Bremhorst, K. & Gilmore, D. B. 1976 *J. Phys.* E: *Sci. Instrum* **9**, 347–352.

Briscolini, M., Santangelo, P., Succi, S. & Benzi, R. 1994 Extended self-similarity in the numerical simulation of three-dimensional homogeneous flows. *Phys. Rev.* E **50**, R1745–R1747.

Brücker, C. 1999 Structure and dynamics of the wake of bubbles and its relevance for bubble interaction flows. *Phys. Fluids* **11**, 1781–1796.

Bruun, H. H. 1995 *Hot Wire Anemometry: Principles and Signal Analysis*. Oxford University Press.

Cartellier, A. 1992 Simultaneous void fraction measurement, bubble velocity, and size estimate using a single optical probe in gas–liquid two-phase flows. *Rev. Sci. Instrum.* **63**, 5442–5453.

Cartellier, A. & Riviere, N. 2001 Bubble-induced agitation and microstructure in uniform bubbly flows at small to moderate particle Reynolds numbers. *Phys. Fluids* **13**, 2165–2181.

Clift, R., Grace, J. R. & Weber, M. E. 1978 *Bubbles, Drops and Particles*. Academics.

Climent, E. & Magnaudet, J. 1997 Simulation d'écoulements induits par des bulles dans un liquide initialement au repos. *C. R. Acad. Sci. Paris* **324**, 91–98.

Climent, E. & Magnaudet, J. 1999 Large-scale simulations of bubble-induced convection in a liquid layer. *Phys. Rev. Lett.* **82**, 4827–4830.

Cui, Z. & Fan, L. S. 2004 Turbulence energy distribution in bubbling gas–liquid and gas–liquid–solid flow systems. *Chem. Engng Sci.* **59**, 1755–1766.

Delhaye, J. M. 1969 Hot-film anemometry in two-phase flow. In *11th ASME/AICHE Heat Transfer Conf. on Two-Phase Flow Instrumentation*, pp. 58–69. Minneapolis, Minnesota: ASME.

Druzhinin, O. A. & Elghobashi, S. 1998 Direct numerical simulations of bubble-laden turbulent flows using the two-fluid formulation. *Phys. Fluids* **10**, 685–697.

Druzhinin, O. A. & Elghobashi, S. 2001 Direct numerical simulation of a three-dimensional spatially developing bubble-laden mixing layer with two-way coupling. *J. Fluid Mech.* **429**, 23–61.

Falkovich, G. 1994 Bottleneck phenomena in developed turbulence. *Phys. Fluids* **6**, 1411–1414.

Farrar, B. & Bruun, H. H. 1989 Interaction effects between a cylindrical hot-film anemometer probe and bubbles in air/water and oil/water flows. *J. Phys.* E: *Sci. Instrum.* **22**, 114–123.

Frisch, U. 1995 *Turbulence*. Cambridge University Press.

Grossmann, S., Lohse, D. & Reeh, A. 1997*a* Application of extended self-similarity in turbulence. *Phys. Rev.* E **56**, 5473.

Grossmann, S., Lohse, D. & Reeh, A. 1997*b* Different intermittency for longitudinal and transversal turbulent fluctuations. *Phys. Fluids* **9**, 3817.

Kohonen, T. 1995 *Self-Organizing Maps*. Springer.

Lance, M. & Bataille, J. 1983 Turbulence in the liquid phase of a bubbly air–water flow. *Proc. of NATO Specialist's Meeting, Spitzensee, Germany*. Martinus Nijhoff.

Lance, M. & Bataille, J. 1991 Turbulence in the liquid phase of a uniform bubbly air–water flow. *J. Fluid Mech.* **222**, 95–118.

Larue de Tournemine, A 2001 Etude experimentale de l'effet du taux de vide en ecoulements diphasiques a bulles. PhD thesis, University of Toulouse.

Lima-Ochoterena, R. & Zenit, R. 2003 Visualization of the flow around a bubble moving in a low viscosity liquid. *Rev. Mex. Fis.* **49**, 348–352.

Ljung, L. 1999 *System Identification: Theory for the User*. Prentice-Hall.

Lohse, D. & Müller-Groeling, A. 1995 The bottleneck effect in turbulence: scaling phenomena in r-space versus p-space. *Phys. Rev. Lett.* **74**, 1747–1750.

Lohse, D. & Müller-Groeling, A. 1996 Anisotropy and scaling corrections in turbulence. *Phys. Rev.* E **54**, 395–405.

Luther, S. & Rensen, J. 2004 Hot-film anemometry in bubbly flow II: Local phase discrimination. *under consideration for publication in Ind. J. Multiphase Flow*.

Luther, S., Rensen, J., van der Berg, T. H. & Lohse, D. 2005 Data analysis for hot-film anemometry in turbulent bubbly flow. *Expl. Therm. Fluid Sci.* **7**, 821–826.

Marié, J. L., Moursali, E. & Tran-Cong, S. 1997 Similarity law and turbulence intensity profiles in a bubbly boundary layer at low void fractions. *Intl J. Multiphase Flow* **23**, 227–247.

Maxey, M., Chang, E. & Wang, L. 1994 Simulation of interactions between microbubbles and turbulent flows. *Appl. Mech. Rev.* **46**, S70–S74.

Mazzitelli, I. & Lohse, D. 2005 The evolution of energy in flow driven through rising bubbles. Preprint 2005.

Mazzitelli, I., Lohse, D. & Toschi, F. 2003*a* The effect of microbubbles on developed turbulence. *Phys. Fluids* **15**, L5–L8.

Mazzitelli, I., Lohse, D. & Toschi, F. 2003*b* On the relevance of the lift force in bubbly turbulence. *J. Fluid Mech.* **488**, 283–313.

Michiyoshi, I. & Serizawa, A. 1984 Turbulence in two-phase bubbly flow. *Proc. Japan US Seminar on two-phase flow dynamics, 29 July – 3 August 3, 1984, Lake Placid, USA.*

Mudde, R. F., Groen, J. S. & van den Akker, H. E. A. 1997 Liquid velocity field in a bubble column: LDA experiments. *Chem. Engng Sci.* **52**, 4217–4224.

Mudde, R. F. & Saito, T. 2001 Hydrodynamical similarities between bubble column and bubbly pipe flow. *J. Fluid Mech.* **437**, 203–228.

Murai, Y. & Matsumoto, Y. 2000 Numerical study of the three-dimensional structure of a bubble plume. *J. Fluid Engng* **122**, 754–760.

Oguz, H. N. & Prosperetti, A. 1993 Dynamics of bubble-growth and detachment from a needle. *J. Fluid Mech.* **257**, 111–145.

Panidis, T. & Papailiou, D. D. 2000 The structure of two-phase grid turbulence in a rectangular channel: an experimental study. *Intl J. Multiphase Flow* **26**, 1369–1400.

Poorte, R. E. G. 1998 On the motion of bubbles in active grid generated turbulent flow. PhD thesis, University of Twente.

Poorte, R. E. G. & Biesheuvel, A. 2002 Experiments on the motion of gas bubbles in turbulence generated by an active grid. *J. Fluid Mech.* **461**, 127–154.

Pope, S. B. 2000 *Turbulent Flow*. Cambridge University Press.

Rensen, J., Luther, S., de Vries, J. & Lohse, D. 2004 Hot-film anemometry in bubbly flow I: Bubble-probe interaction. *Intl J. Multiphase Flow* **31**, 285–301.

Saito, N. & Coifman, R. R. 1994 Local discriminant bases. In *Wavelet Applications in Signal and Image Processing II, Proc. SPIE 2303* (ed. A. F. Laine & M. A. Unser), pp. 2–14.

Serizawa, A. & Kataoka, I. 1995 Dispersed flow. In *Multiphase Science and Technology, vol. 8. Two-phase flow fundamentals* (ed. G. F. Hewitt, J. H. Kim, R. T. Lahey, J. M. Delhaye & N. Zuber), pp. 125–194 (chap. 3). Begell House.

Serizawa, A., Kataoka, I. & Michiyoshi, I 1975 Turbulence structure of air–water bubbly flow – II Local properties. *Intl J. Multiphase Flow* **2**, 235–246.

Serizawa, A., Tsuda, K. & Michiyoshi, I. 1983 Real-time measurement of two-phase flow turbulence using a dual-sensor anemometry. In *Proc. Symp. on Measuring Techniques in Gas–Liquid Two-Phase Flows* (ed. J. M. Delhaye & G. Cognet), *Nancy, France*, pp. 495–523. Springer.

Sreenivasan, K. R. & Antonia, R. A. 1997 The phenomenology of small-scale turbulence. *Annu. Rev. Fluid Mech.* **29**, 435–472.

Tabeling, P., Zocchi, G., Belin, F., Maurer, J. & Willaime, H. 1996 Probability density functions, skewness and flatness in large Reynolds number turbulence. *Phys. Rev.* E **53**, 1613.

Veldhuis, C. H. J., Biesheuvel, A., van Wijngaarden, L. & Lohse, D. 2005 Wake structure of a rising spherical particle. *Nonlinearity* **18**, C1–C8.

de Vries, A. W. G., Biesheuvel, A. & van Wijngaarden, L. 2002*a* Notes on the path and wake of a gas bubble rising in pure water. *Intl J. Multiphase Flow* **28**, 1823–1835.

de Vries, J., Luther, S. & Lohse, D. 2002*b* Induced bubble shape oscillations and their impact on the rise velocity. *Eur. Phys. J.* B **28**, 503–509.

Wang, G. & Ching, C. Y. 2001 Measurement of multiple gas-bubble velocities in gas-liquid flows using hot-film anemometry. *Exps. Fluids.* **31**, 428–439.

Wang, S. K., Lee, S. J., Jones, O. C. & Lahey, R. T. 1990 Statistical analysis of turbulent two-phase pipe flow. *J. Fluid Engng* **112**, 89–95.

Wang, L. & Maxey, M. 1993 The motion of microbubbles in a forced isotropic and homogeneous turbulence. *Appl. Sci. Res.* **51**, 291–296.

Welch, P. D. 1967 The use of fast Fourier-transform for the estimation of power spectra: a method based on time averaging over short, modified periodograms. *IEEE Trans. Audio Electroacoust.* **AU-15**, 70–73.

van Wijngaarden, L. 1998 On pseudo turbulence. *Theor. Comput. Fluid Dyn.* **10**, 449–458.